

Processes controlling surface, bottom and lateral melt of Arctic sea ice in a state of the art sea ice model

Article

Accepted Version

Tsamados, M., Feltham, D., Petty, A., Schroeder, D. and Flocco, D. (2015) Processes controlling surface, bottom and lateral melt of Arctic sea ice in a state of the art sea ice model. *Philosophical Transactions of the Royal Society A: Mathematical, Physical and Engineering Sciences*, 373 (2052). 20140167. ISSN 1364-503X doi: <https://doi.org/10.1098/rsta.2014.0167> Available at <http://centaur.reading.ac.uk/57187/>

It is advisable to refer to the publisher's version if you intend to cite from the work.

Published version at: <http://dx.doi.org/10.1098/rsta.2014.0167>

To link to this article DOI: <http://dx.doi.org/10.1098/rsta.2014.0167>

Publisher: Royal Society Publishing

All outputs in CentAUR are protected by Intellectual Property Rights law, including copyright law. Copyright and IPR is retained by the creators or other copyright holders. Terms and conditions for use of this material are defined in the [End User Agreement](#).

www.reading.ac.uk/centaur

CentAUR

Central Archive at the University of Reading

Reading's research outputs online

1 ¹Centre for Polar Observation and Modelling, Department of Meteorology, University of
2 Reading, Reading, UK.

3 ²Centre for Polar Observation and Modelling, Department of Earth Sciences, University
4 College London, London, UK.

5 ³Earth System Science Interdisciplinary Center, University of Maryland, College Park, MD,
6 USA

7 Climate Model, Sea ice, Arctic
8 Sea ice model, Melt, Processes

9 Michel Tsamados

10 m.tsamados@ucl.ac.uk

11 ABSTRACT

12 We present a modelling study of processes controlling the summer melt of the Arctic sea
13 ice cover. We perform a sensitivity study and focus our interest on the thermodynamics
14 at the ice-atmosphere and ice-ocean interfaces. We use the Los Alamos community sea ice
15 model CICE, and additionally implement and test three new parameterization schemes: (i)
16 a prognostic mixed layer; (ii) a three equation boundary condition for the salt and heat flux
17 at the ice-ocean interface; and (iii) a new lateral melt parameterization. Recent additions to
18 the CICE model are also tested, including explicit melt ponds, a form drag parameterization,
19 and a halodynamic brine drainage scheme.

20 The various sea ice parameterizations tested in this sensitivity study introduce a wide
21 spread in the simulated sea ice characteristics. For each simulation, the total melt is decom-
22 posed into its surface, bottom and lateral melt components to assess the processes driving
23 melt and how this varies regionally and temporally. Because this study quantifies the relative
24 importance of several processes in driving the summer melt of sea ice, this work can serve
25 as a guide for future research priorities.

26 Processes controlling surface, bottom and lateral melt of
27 Arctic sea ice in a state of the art sea ice model

28 Michel Tsamados^{1,2}, Daniel Feltham¹, Alek Petty³,
David Schroeder¹ and Daniela Flocco¹

29 April 12, 2016

30 **1. Introduction**

31 The Arctic sea ice cover has undergone a rapid decrease in extent (e.g. Stroeve et al.
32 2012) and thickness (Kwok et al. 2009; Laxon et al. 2013; Lindsay and Schweiger 2015) over
33 recent decades; transitioning from a predominantly multi-year ice pack to an increasingly
34 seasonal ice pack (e.g. Comiso 2011). This decline has been accompanied by increases in
35 sea ice drift (Rampal et al. 2009; Spreen et al. 2011) and deformation (Rampal et al. 2011)
36 over a similar time period. The drastic regime shift observed in recent years suggests that
37 the sea ice models developed following the early field campaigns of the 1960s/1970s (Arctic
38 Ice Dynamics Joint Experiment, AIDJEX), and the 1990s (Surface Heat Budget of the
39 Arctic Ocean, SHEBA) need to be re-evaluated against current sea ice conditions (Notz
40 2012). Some of the assumptions in these early models have since been challenged, both in
41 their thermodynamic (Feltham et al. 2006; McPhee 2012) and dynamic (Coon et al. 2007;
42 Feltham 2008) components. In this study we seek to understand the processes controlling the
43 summer melt of Arctic sea ice, and thus we focus our attention on the various thermodynamic
44 parameterization schemes included in a state of the art sea ice model.

45 Large regional and temporal variability in the sea ice state and the oceanic/atmospheric
46 forcing provides a significant challenge when trying to assess the various processes that
47 contribute to Arctic sea ice melt. In addition, *in-situ* measurements that provide a decom-
48 position of sea ice melt processes (top, bottom and lateral melt) are sparse (Richter-Menge
49 et al. 2006; Toole et al. 2011). Recently, (Perovich et al. 2014) quantified the relative im-
50 portance of surface ice/snow melt and bottom ice melt using autonomous Ice Mass Balance
51 buoys (IMB) deployed over more than ten years (2000 to 2013) that drifted from the North
52 Pole towards the Fram Strait. The study found surface and bottom melt to be of a similar
53 magnitude on average, although both exhibited large inter-annual and regional variability.
54 The study also demonstrated an almost doubling of bottom melt over the period 2008 to
55 2013 with respect to the period 2000 to 2005. Measurements of lateral melt are lacking and
56 parameterizations of lateral melt in sea ice models are based on observations taken in the
57 1980s (e.g. Steele (1992) and references therein). The contribution to total Arctic sea ice
58 melt from lateral melt is thought to be small in comparison to bottom and surface melt over
59 high concentration areas, meaning its impact is mainly limited to the marginal ice zone. The
60 increased areal coverage of the summertime marginal ice zone over recent years (Strong et al.
61 2013) could, however, be increasing the relative importance of lateral melt on a basin scale.

62 Sensitivity studies of one dimensional models of sea ice have been used in the past to
63 assess the relative importance of different processes in driving the sea ice response to a
64 prescribed external forcing in the Arctic (Ebert and Curry 1993) and in the Antarctic (Petty
65 et al. 2012). These approaches are helpful in understanding the mean behaviour of the
66 sea ice system but fail to capture the spatio-temporal complexity of the sea ice response
67 and ignore feedbacks between the atmosphere, ice and ocean. At the other end of the
68 complexity spectrum, ice-ocean (IO) coupled models (Johnson et al. 2007) and fully coupled
69 atmosphere-ice-ocean (AIO) models (Maslowski et al. 2012; Keen et al. 2013; Rae et al.
70 2014), can resolve the regional and temporal sea ice response and feedback processes but
71 are computationally expensive and often remain too simplified in representing the physics of

72 sea ice. As a compromise between physical complexity and computational expense, we use a
73 stand-alone sea ice model coupled to a prognostic ocean mixed layer (denoted ML hereafter)
74 model to quantify the impact of various new physical processes on the sea ice system while
75 retaining realistic regional information.

76 The total volume of sea ice within the Arctic basin is controlled by a balance between a
77 thermodynamic (growth/melt) and a dynamic (ice import/export) contribution (Hibler et al.
78 2006). Locally, the sea ice thickness is controlled by the balance of heat conduction ($F_{condbot}$,
79 $F_{condtop}$, see figure 1) and incoming fluxes (F_{ice} , F_{surf} , see figure 1) at its upper and lower
80 surfaces. As illustrated by simple one-dimensional models (Ebert and Curry 1993), the mean
81 sea ice thickness (and by extension the total volume of ice) is sensitive to the external forcing
82 (e.g. temperature, humidity, wind, incoming radiation, ocean heat flux) as well as to the
83 parameterizations used to describe the sea ice thermodynamic processes (e.g. albedo scheme,
84 lead opening, snow and ice thermal properties, treatment of the interfaces). In our stand-
85 alone setup, the external forcing is to a large degree constrained by the reanalysis. However,
86 the use of a prognostic melt pond scheme (Flocco et al. (2012)) modifies the incoming
87 shortwave radiation at the ice-atmosphere interface and the inclusion of the Petty et al.
88 (2014) prognostic ML model alters the basal ice-ocean flux and allows feedbacks between
89 the ice and the ML. Therefore, even with prescribed boundary conditions and a stand-alone
90 sea ice model, the heat budget of the Arctic sea ice (figure 2 a) and ML (figure 2 b) can be
91 substantially modified by the choice of parameterization schemes used.

92 To better understand the physical mechanisms affecting the large scale retreat of the
93 summer Arctic sea ice cover and the relative importance of lateral melt, basal melt and
94 surface melt, we perform in this paper a sensitivity study of the summer sea ice state and
95 melt to different sea ice physics parameterization schemes. The various model runs are
96 analysed both in terms of their local response to a prescribed external forcing (melt rates,
97 interface temperature, salinity and fluxes) as well as their basin scale ice state characteristics
98 (total extent, area and volume).

99 The paper is structured as follows: section 2 presents the model setup, the sensitivity
100 studies and the various physical processes assessed in this study; section 3 discusses the
101 model results, the impact on the sea ice state characteristics, the mixed layer properties,
102 and the relative importance of top, bottom and lateral melt in the model; and finally, a
103 discussion and concluding remarks are given in section 4.

104 **2. Processes controlling ice melt in a sea ice model**

105 *a. Choice of model configuration*

106 We use version 5.0.2 of the Los Alamos sea ice model, CICE, described in detail by
107 Hunke et al. (2013). This state of the art sea ice model includes a large number of physical
108 parameterization schemes that can be turned on or off by the user. Here we briefly describe
109 the schemes tested in this study.

110 The model uses multiple ice-thickness categories compatible with the ice thickness redis-
111 tribution scheme of Lipscomb et al. (2007). We set the number of ice thicknesses to 5 and set
112 the mean ridge height (a tunable parameter) to $\mu_{rdg} = 4 \text{ m}^{1/2}$ (Hunke et al. 2013). We also
113 use the default incremental remapping advection scheme of Lipscomb and Hunke (2004).

114 In all model runs we choose the elastic-anisotropic-plastic (EAP) rheology described in
115 Tsamados et al. (2013). This rheology is the default choice in our developmental branch
116 of CICE and was shown to result in large regional differences in ice thickness with respect
117 to the default elastic-viscous-plastic (EVP) rheology of Hunke and Dukowicz (2002). We
118 choose the ice strength formulation of Rothrock (1975) and set the empirical parameter that
119 accounts for frictional energy dissipation to $C_f = 17$.

120 CICE contains three explicit melt pond parameterizations (Hunke et al. 2013) that are
121 used in conjunction with the Delta-Eddington radiation scheme (Briegleb and Light 2007).
122 In all our runs we use the physically based melt pond model of Flocco et al. (2012) which
123 simulates the evolution of melt ponds based on sea ice conditions and external forcing.

124 In this latest version of CICE, the vertical temperature and salinity profiles as well as
 125 the brine volume are calculated. We choose to resolve five ice layers and one snow layer
 126 vertically and compare model results between the fixed salinity profile parameterization of
 127 Bitz and Lipscomb (1999) and the newly available mushy parameterization, in which the
 128 salinity within the ice can evolve in time (halodynamic model of Turner et al. (2013)). The
 129 differences between the two models as well as the impact of both halodynamic components
 130 on the main sea ice characteristics are discussed in details in Turner and Hunke (2015).

131 At the ice-ocean interface, we use the ocean heat flux formulation of Maykut and McPhee
 132 (1995), $F_{ice} = \rho_w c_p \alpha_h u_* \Delta T$, ρ_w the water density, c_p the specific heat for seawater near
 133 freezing and α_h the Stanton number or sensible heat transfer coefficient. The friction velocity
 134 is calculated as $u_* = \sqrt{\tau_w / \rho_w}$, where τ_w is the ice-ocean drag (including form drag when
 135 calculated (Tsamados et al. 2014)). Finally the temperature difference is taken as $\Delta T =$
 136 $T_{mix} - T_0$, with T_{mix} the mixed layer temperature and T_0 the temperature at the ice-ocean
 137 interface. As a default in CICE, T_0 is chosen equal to the freezing temperature of water at
 138 the salinity of the mixed layer, $T_0 = T_F(S_{mix})$.

139 In the default CICE setup both atmospheric (ANDC) and oceanic (ONDC) neutral drag
 140 coefficients are assumed constant in time and space. Following Tsamados et al. (2014) and
 141 based on recent theoretical developments (Lu et al. 2011; Lüpkes et al. 2012) the total
 142 neutral drag coefficients can now be estimated from properties of the ice cover such as ice
 143 concentration, vertical extent and area of the ridges, freeboard and floe draft, and size of
 144 floes and melt ponds. The new parameterization allows the drag coefficients to be coupled
 145 to the sea ice state and therefore to evolve spatially and temporally. For more detail on the
 146 implementation we refer the reader to Tsamados et al. (2014). Note that in contrast to the
 147 earlier implementations of form drag in Tsamados et al. (2014) or Hunke (2014) we set the
 148 Stanton coefficient, α_h , to be proportional to the oceanic neutral drag coefficient, C_{dw} .

149 As a default setting we choose $\alpha_h = C_{dw}/2$, to be consistent with airborne measurements
 150 of neutral drag coefficients for heat and momentum over the Arctic sea ice (see for example

151 Schröder et al. (2003), Figure 6 b). Note that during the melt season when false bottoms
 152 (or any accumulation of low salinity water at the ice-ocean interface) cover a sufficiently
 153 large portion of the pack ice and limit bottom heat flux, reducing the parameter α_h can
 154 be qualitatively justified. As a simple representation of false bottoms, we therefore modify
 155 the ice-ocean heat transfer coefficient according to the melt pond concentration at the ice
 156 surface.

157 For lateral melt we use the parameterization of Maykut and Perovich (1987) and Steele
 158 (1992) as implemented in CICE

$$\frac{\partial A}{\partial t} = -w_{lat} \frac{\pi}{\alpha L} A, \quad (1)$$

159 where A is the sea ice concentration, L is the typical floe diameter (set as a default in
 160 CICE to $L = 300$ m), α is a geometrical parameter, and w_{lat} is the lateral melting rate,
 161 parameterized as in Perovich (1983), $w_{lat} = m_1 \Delta T^{m_2}$ ($m_1 = 1.6$, $m_2 = 1.36$).

162 We now describe the implementations that are currently unique to our developmental
 163 branch of CICE.

164 *b. Additional processes implemented in this study*

165 *(i) Prognostic mixed layer model in the Arctic*

166 The default stand-alone configuration in CICE uses a fixed slab ocean mixed layer (ML)
 167 with a prognostic ML temperature, T_{mix} , but a prescribed ML salinity from climatology,
 168 S_{mix} , and a constant ML depth, $h_{mix} = 20$ m. Here we include the bulk ML model of Petty
 169 et al. (2014) that was used to investigate shelf water formation around Antarctica. This
 170 simple prognostic mixed layer model allows the temperature but also the salinity and the
 171 depth of the ML to evolve under the influence of surface and deep-ocean heat/salt fluxes.
 172 The model is based on the turbulent energy budget approach of Kraus and Turner (1967),
 173 which assumes that temperature and salinity are uniform throughout the mixed layer, and

174 that there is a full balance in the sources and sinks of turbulent kinetic energy. The ML
 175 entrainment rate is then calculated by balancing the power needed to entrain water from
 176 below with the power provided by the wind and the surface buoyancy fluxes (see Petty et al.
 177 (2014) for further details about this model choice).

178 At the surface the mixed layer receives a heat flux from the ice ($F_{ice} + F_{swthru}$, figure
 179 1) and open-ocean fractions ($F_{s/w}$, figure 1) (all fluxes are positive downwards) and a salt
 180 flux calculated in CICE as a combination of ice/snow growth/melt (F_{ice}^S , figure 1) and pre-
 181 cipitation and evaporation (F_{pe}^S , figure 1) (note that the rainfall and melt water on sea ice
 182 is assumed to percolate through the sea ice and enters the ML). In the winter as the ML
 183 deepens, heat and salt from the ocean below at the temperature, T_b , and salinity, S_b , are
 184 entrained in the ML (respectively fluxes, F_{bot} and F_{bot}^S , figure 1), while in the summer as the
 185 ML shallows and leaves behind a layer of Winter Water there are no heat or salt fluxes at
 186 the bottom of the ML. In our implementation we introduce a minimum ML depth, h_{mix}^{min} ,
 187 and assume that there are no heat and salt exchanges between the ML and the ocean below
 188 when the ML reaches this minimum.

189 We apply a slow ($\tau_r = 20$ days) temperature restoring of the ML temperature towards
 190 a monthly climatology of the 10 m depth reanalysis temperature taken from MYO-WP4-
 191 PUM-GLOBAL-REANALYSIS-PHYS-001-004 reanalysis (Ferry et al. 2011) (hereafter noted
 192 MYO). This temperature restoring can be seen as a parameterization of the advection of heat
 193 in the upper ocean. The weak temperature restoring is consistent with model results from
 194 a coupled ice-ocean model (Steele et al. 2010) that found in the Arctic advection under the
 195 pack ice to be relatively small in comparison with surface heat fluxes. To represent oceanic
 196 heat flux convergence melting sea ice at the ice edge (Bitz et al. 2006), we adopt a faster
 197 temperature restoring ($\tau_r=2$ days) when $T_{mix} > T_{mix}^{MYO} + 0.2$. Note that the value of 0.2°
 198 C is large enough to ensure that the fast restoring mainly occurs in the winter around the
 199 ice edge. This ad-hoc method is equivalent to applying an additional heat flux to the ML,
 200 $F_{adv} = (T_{mix} - T_{mix}^{MYO}) / (\tau_r \rho_w c_p h_{mix})$ (see figure 1 a). The fast temperature restoring is mostly

201 important in controlling the winter sea ice extent while the slow temperature restoring acts
202 as a heat sink for the ML in the summer.

203 In addition to this temperature restoring we use a slow (365 days) restoring to the sea
204 surface salinity in the ML. In our new prognostic ML setup the freezing temperature of the
205 mixed layer is updated to account for the modified salinity of the ML. As the ML shallows
206 at the onset of melt, Winter Water is left behind in the deep ocean grid. The deep ocean
207 salinity and temperature are then slowly restored with a time scale of 1 year to a winter
208 (January 1st) climatology (1993-2010) from the MYO reanalysis. The ocean properties below
209 the mixed layer are therefore relaxed towards observed climatology; isolating the effect of
210 surface forcing and allowing us to understand short term (seasonal) variations in the ML.

211 *(ii) Lateral melting and floe size distribution*

212 We generalize the lateral melt parameterization of equation (1) to account for a power
213 law distribution of floe sizes, in order to be consistent with observations (e.g. Herman (2010)
214 and references therein). In our new lateral melt parameterization scheme, the variable L in
215 equation (1) represents the average floe size instead of representing a unique floe size as in
216 the default lateral melt scheme.

217 For typical winter pack ice $L \geq 100$ m (Weiss and Marsan 2004) and lateral melting is
218 negligible in comparison to bottom and surface melting (Steele et al. 1989). In summer, the
219 average floe size decreases and the relative importance of lateral melting to basal melting
220 increases as the ratio of perimeter to area increases. Wave-ice interaction fractures the ice
221 and leads to smaller floes in the marginal ice zone. The average floe size typically varies
222 with the ice concentration and was parameterized in the marginal ice zone by Lüpkes et al.
223 (2012) to be:

$$L = L_{min} \left(\frac{A_{\star}}{A_{\star} - A} \right)^{\beta}, \quad (2)$$

224 where A_{\star} is introduced instead of the value 1 to avoid a singularity at $A = 1$, the exponent β

225 is chosen in the range 0.2 to 1.4 ($\beta = 0.5$ in this study), and L_{min} is a characteristic minimal
 226 floe size ($L_{min} = 8\text{m}$ in this study). Here, we have extended this parameterization to the
 227 entire ice cover, but note that in the case where $L \geq 100$ m the contribution from lateral
 228 melting becomes negligible and the floe size parameterization becomes irrelevant to lateral
 229 melt.

230 In the appendix we show that if one uses a power law floe size distribution, then the
 231 total lateral melt is reduced relatively to the situation with a unique floe size. Lateral melt
 232 is reduced by a factor $P_0(\zeta)$ applied to the right hand side of equation (1),

$$\frac{\partial A}{\partial t} = -P_0(\zeta)w_{lat}\frac{\pi}{\alpha L}A, \quad (3)$$

233 where ζ is the power exponent of the power law distribution $n_r(r)$, with $\frac{n_r(r)}{\pi r^2}$, being the
 234 number of floes of size r per unit area. Typical observed values of ζ are in the range 1 to
 235 2 with the corresponding values of the attenuation pre-factor, respectively $P_0(1) = 0$ and
 236 $P_0(2) = 0.75$. In this study we choose $\zeta = 1.13$ and $P_0(1.13) = 0.2$. We should note that the
 237 choice of the exponent ζ is subjective and needs to be constrained further from observations.

238 *(iii) Three equation boundary conditions*

239 The Maykut and McPhee (1995) formulation of the heat flux from the ocean into the ice,
 240 F_{ice} (see section 2a), depends on the interfacial temperature, T_0 . As discussed in Schmidt
 241 et al. (2004), the interfacial temperature can be chosen in models as: (i) a constant freezing
 242 temperature of sea water (typically sea water at a salinity of 34 PSU); (ii) the freezing
 243 temperature of the ML (default option in CICE); or (iii) the freezing temperature, T_f , of the
 244 sea water directly below the sea ice with the interfacial salinity, S_0 , that in the summer can
 245 be fresher than the water in the ML due to the freshwater fluxes associated with melting.
 246 In this latter case one must solve the following system of three equations described in Notz
 247 (2005) and McPhee (2008):

$$-F_{condbot} + \rho_w c_p \alpha_h u_0^* (T_{mix} - T_0) - q \dot{h}_0 = 0, \quad (4)$$

$$\alpha_s u_0^* (S_{mix} - S_0) + \dot{h}_0 (S_{ice} - S_0) = 0, \quad (5)$$

$$T_0 = T_f(S_0) \simeq -m S_0, \quad (6)$$

248 where $F_{condbot}$ is the downward ice conductive heat flux at the basal surface, q is the enthalpy
 249 of new ice forming with the salinity and freezing temperature of the sea surface and \dot{h}_0 is the
 250 rate of ice growth at the ice-ocean interface. T_{mix} and S_{mix} are respectively the temperature
 251 and salinity of the mixed layer. The exchange coefficients for salinity and heat are different
 252 under melting conditions, $\alpha_s = \alpha_h/50$ and under freezing conditions, $\alpha_s = \alpha_h$ (McPhee
 253 2008).

254 Note that this is a new parameterization scheme included in CICE. We solve the system
 255 of equations (4)-(6) separately for each ice thickness category and save T_0 , S_0 as well as all
 256 fluxes as output variables. Note that this parameterization scheme is only operational in
 257 CICE when the mushy layer parameterization of Turner et al. (2013) is switched on.

258 *c. Reference model run and sensitivity model runs*

259 We describe in this section our chosen reference run and model sensitivity runs. Our
 260 ambition is not to find an optimal model configuration but instead to test the impact of the
 261 model physics on a sufficiently realistic model configuration. The reference configuration
 262 follows largely from previous work by Tsamados et al. (2014) and Schröder et al. (2014) that
 263 included several recent model developments (see section 2a) and was able to demonstrate
 264 good agreement to the observed September sea ice extent. In addition our reference model
 265 configuration was chosen to reproduce reasonably well the main sea ice characteristics in the
 266 summer months, in particular the sea ice concentration in August that is often underesti-
 267 mated in models (Notz 2013). Because they are implemented in CICE for the first time, we
 268 focus in particular in our sensitivity study on the processes described in section 2b.

269 In the reference run, *REF*, most model implementations described in sections 2a and b
270 are switched on, namely: the prognostic mixed layer of Petty et al. (2014); the three equation
271 boundary condition treatment of the ice-ocean interface; the mushy layer thermodynamic
272 implementation of Turner et al. (2013); the form drag parameterization of Tsamados et al.
273 (2014); a heat transfer coefficient proportional to the oceanic neutral drag coefficient, $\alpha_h =$
274 $C_{dw}/2$. On the other hand the new lateral melt parameterization is not used.

275 In addition to the *REF* run we perform a series of sensitivity runs. We adopt for each
276 physical process a simple on-off approach where each additional model run contains a sim-
277 ple modification with respect to the *REF* run. The names and changes in these sensi-
278 tivity runs are as follows. In *MLD_CST* we use the default fixed depth slab ocean ML
279 described in 2i); in *MLD_MIN_2M* we set the minimum allowed ML depth to $h_{mix} = 2$ m;
280 in *NO_3EQTN* we revert to the default boundary condition treatment with $T_0 = T_f(S_{mix})$
281 (see 2iii); in *NO_MUSHY* we replace the mushy parameterization and flushing of Turner and
282 Hunke (2015) by the fixed salinity profile scheme of Bitz and Lipscomb (1999) (section 2a);
283 *DBL_ALPHA_H*, *DBL_ALPHA_H / NO_3EQTN* and *DBL_ALPHA_H / NO_MUSHY* are
284 the same as *REF*, *NO_3EQTN* and *NO_MUSHY* but with a doubling of α_h (section 2a); in
285 *NO_POND* we artificially set the thickness of the melt ponds to zero; in *FALSE_BOTTOM*
286 to simply model the impact of under ice fresh water accumulation on the bottom heat flux we
287 double α_h where melt ponds cover more than 20% of the ice surface; in *NO_FORM_DRAG* we
288 switch off the Tsamados et al. (2014) form drag parameterization (section 2a); in *LAT_MELT*
289 we switch on the lateral melt parameterization described in section 2b; finally in *SST_TIME*
290 we restore the sea surface temperature to the time dependent temperature of the MYO
291 reanalysis surface ocean temperature over the period 1993 to 2010 (because the ocean re-
292 analysis is limited to this period). All the sensitivity runs are summarized in table 1.

293 All simulations are run in stand-alone mode on a 1° tripolar (129×104) grid that covers
294 the whole Arctic Ocean (note that the Hudson Bay and part of the Canadian Archipeleago
295 are treated as land) with a horizontal grid resolution of around 50 km. Atmospheric forcing

296 data are taken from the NCEP-NCAR reanalysis (Kanamitsu et al. 2002): 6-hourly 10-m
297 winds, 2-m temperatures and 2-m humidity, daily shortwave and longwave radiation as well
298 as monthly snowfall and precipitation rates. Sea surface temperature (SST) and salinity
299 (SSS) are taken from the MYO reanalysis (Ferry et al. 2011) to initialize the Arctic sea ice
300 state. Climatological monthly means from Ferry et al. (2011) are used for the ocean currents
301 (depth of 10 m). Starting with an homogeneous sea ice with thickness of 2.5 m, a snow
302 depth of 20 cm and a concentration of 100% the reference model, REF, is spun up for 10
303 years (1980-1989) once. This configuration is used as initial condition for all the simulation
304 runs described in table 1 that are then run for a period of 24 years (1990-2013).

305 **3. Results of a sensitivity study**

306 *a. Relative importance of top, bottom and lateral melt*

307 In this section we describe the impact of the various parameterization schemes on the
308 summer Arctic sea ice-mixed layer state. Figure 3 shows the mean seasonal and inter-annual
309 mixed layer temperature T_{mix} (figure 3 a and b), mixed layer salinity S_{mix} (figure 3 e and f),
310 and mixed layer depth h_{mix} (figure 3 i and j) for each model simulation. To decompose the
311 thermodynamic response of each model simulation and to quantify the relative importance
312 of top, bottom and lateral melt, figure 3 shows the mean seasonal and inter-annual surface
313 melt rate (figure 3 c and d), bottom melt rate (figure 3 g and h) and lateral melt rate (figure
314 3 k and l).

315 Looking first at the mean upper ocean characteristics, we see that the seasonal cycle of
316 h_{mix} is important in controlling the temperature and salinity of the ML. From a simple heat
317 and salt conservation argument (equations 14 and 15 in Petty et al. (2014)) the shallowing of
318 the ML in the summer season results in an increase of the average T_{mix} (figure 3 a), from an
319 average maximum in July of $\sim -1.0^\circ\text{C}$ in *MLD_CST* to $\sim -0.8^\circ\text{C}$ in *REF* and $\sim -0.5^\circ\text{C}$
320 in *MLD_MIN_2M* and a reduction of the average minimum SSS in July (figure 3 e) from

321 ~ 31.3 PSU to ~ 29 PSU and ~ 27.4 PSU. In addition to the seasonal dependence the ML
 322 appears to be warming (figure 3 b) and freshening (figure 3 f) over the last 2 decades in
 323 July and this trend is stronger for the shallower summer ML in *MLD_MIN_2M*. Interestingly,
 324 despite having a thicker h_{mix} , *NO_MUSHY* displays very similar T_{mix} characteristics as in
 325 *MLD_MIN_2M*. This reflects the additional incoming solar radiation in this model run that
 326 was shown by Turner and Hunke (2015) to be related to the reduced flushing rate in the Bitz
 327 and Lipscomb (1999) parameterization resulting in a larger pond area fraction and a lower
 328 albedo. The summer T_{mix} climatology in *NO_3EQTN*, *NO_FORM_DRAG*, *NO_POND* and
 329 *SST_TIME* is lower than *REF* by approximately 0.1°C . Note also that in *SST_TIME* there
 330 is a strong warming trend of the ML and the interannual variability of T_{mix} is much larger
 331 than in *REF*. This points to the importance of the oceanic temperature restoring scheme
 332 used in a stand-alone setting. These variations in the mean ML characteristics can help us
 333 explain the differing bottom and lateral melt rates from each simulation as discussed next.

334 The bottom and lateral heat fluxes scale respectively with ΔT and ΔT^{m_2} ($\Delta T = T_{mix} -$
 335 T_0 , see section 2c). Intuitively one might therefore expect a higher summer T_{mix} will con-
 336 tribute to an increase in the bottom and lateral heat flux. However, a fresher ML results in
 337 an increased freezing temperature at the ice-ocean interface (here we assume $T_0 = T_F(S_{mix})$)
 338 which will reduce the bottom and lateral heat flux. Comparing *MLD_CST* and *REF* in
 339 figure 3 g and h, we can see that despite the higher T_{mix} in the *REF* simulation, the im-
 340 pact on the average local bottom melt is negligible. In the *MLD_MIN_2M* and *NO_MUSHY*
 341 simulations, however, the increase in T_{mix} compared to *REF* appears sufficient to cause
 342 a significant increase in the bottom and lateral melt (see figure 3 h and l). Finally, the
 343 *NO_3EQTN* simulation demonstrates the insulating effect caused by switching on the three
 344 equation boundary conditions. Indeed despite the higher T_{mix} throughout summer in the
 345 *REF* simulation, the bottom melt rate is significantly higher on average for *NO_3EQTN*.
 346 This can only be explained by the larger interfacial temperature in *REF* (not shown) that,
 347 in contrast to *NO_3EQTN*, is taken as the freezing temperature of the fresher water directly

348 below the sea ice (see equations (4)-(6)).

349 The mean seasonal (figure 3 (c), (g) and (k)) and annual time-series (figure 3 (d), (h)
350 and (l)) of the basin average surface, bottom and lateral melt rates show that the bottom
351 melt is the strongest contributor to the total melt (up to ~ 1.5 cm/day in July for *REF*).
352 The top melt is the second strongest contribution (up to ~ 1.25 cm/day in July for *REF*)
353 and, as expected, is largely insensitive to modifications to the ML. Except in the case of the
354 floe size dependent lateral melt parameterization, *LAT_MELT*, the contribution from lateral
355 melt is on average small (up to ~ 0.25 cm/day in July for *REF*). For the *REF* simulation
356 in July, surface melt shows the highest interannual variability, with a standard deviation of
357 0.41 cm/day (figure 3 d), compared with 0.29 cm/day for bottom melt (figure 3 h) and 0.06
358 cm/day for lateral melt (figure 3 l). These results suggest that in our model implementation,
359 interannual variability of the summer sea ice characteristics (area, extent, volume) will be
360 dominated by the surface melt processes. This could explain why the inclusion of a realistic
361 description of surface melt ponds in CICE results in significant skill in reproducing and
362 forecasting the September sea ice extent (Schröder et al. 2014). Note also that the lower
363 interannual variability in *REF* (0.29 cm/day) compared to *SST_TIME* (0.36 cm/day) could
364 indicate that the simulations without temperature restoring to a time dependent reanalysis
365 might underestimate the true variability of the upper ocean temperature and salinity.

366 Figure 4 decomposes the changes in the total volume of ice into its various thermody-
367 namic components during ice growth (congelation growth, frazil ice formation and snow
368 ice formation) and ice melt (surface melt, bottom melt and lateral melt). Figure 4 shows
369 that the mean annual ice growth is dominated in all sensitivity simulations by congela-
370 tion growth ($+9500\text{km}^3$ in *REF*), followed by frazil ice formation ($+4100\text{km}^3$ in *REF*), and
371 snow ice formation ($+800\text{km}^3$ in *REF*). The mean annual ice melt is dominated by bot-
372 tom melt (-10000km^3 in *REF*), followed by surface melt (-3200km^3 in *REF*) and lateral
373 melt (-1200km^3 in *REF*). In all the simulations, the total annual ice melt and growth
374 largely cancel each other out over the full annual cycle, leaving only a small negative term

375 associated with the expected ice volume decline over the 1993 to 2010 period. The differ-
376 ences in the mean total sea ice volume across all simulations occurs in a transient period of
377 up to five years from 1990 to 1994 (not shown). Three simulations stand out in figure 4,
378 *NO_MUSHY*, *LAT_MELT* and *SST_TIME*. Relative to *REF*, *NO_MUSHY* shows an overall
379 increase in congelation growth (+3750km³) and a reduction in surface melt (-900km³) and
380 lateral melt (-200km³), compensated by a decrease in frazil ice formation (-3100km³) and
381 an increase in snow ice formation (+850km³) and bottom melt (+950km³). The increase in
382 lateral melt in *LAT_MELT* (-2500km³) is largely compensated by a reduction in bottom
383 melt (+2200km³) reflecting the fact that the heat available in the ML to melt the ice from
384 below is divided between lateral and bottom melt. In *SST_TIME*, a large increase in frazil
385 ice formation is compensated by less congelation growth and increased bottom melt. These
386 compensating effects are examples of the negative feedback processes that take place during
387 the thermodynamic cycle of sea ice.

388 Decomposing the total ice melt shows that bottom melt accounts for more than two
389 thirds of the total ice melt, top melt accounts for almost a third of the total and lateral
390 melt contributes less than 10%. Looking at the ice melt across individual months (not
391 shown) shows that a significant fraction of the total bottom melt occurs outside the summer
392 melt season (from September to April), featuring monthly ice melt volumes of -2000km³
393 to -5000km³. Over the same monthly time period, the contribution to the total melt from
394 surface and lateral melt is small. Looking at maps of ice melt (similar to figure 6) for
395 the September to April months (not shown) demonstrates that this ‘winter’ bottom melt
396 contribution occurs mainly around the ice edge, driven by warm southern Atlantic and
397 Pacific waters. In the *REF* simulation, the monthly (inter-annual) mean ice melt in June,
398 July and August is -6000km³, -28000km³ and -5000km³ for surface melt, -22000km³,
399 -38000km³ and -22000km³ for bottom melt and -4000km³, -5000km³ and -3000km³ for
400 lateral melt.

401 We now look at the spatial pattern of the surface (figure 5), bottom (figure 6) and lateral

402 (figure 7) melt for each simulation for July (the maximum melt month). In these figures,
403 absolute melt rates are shown for *REF*, while relative values are shown for all other model
404 runs. Looking first at the absolute values of the melt rates in *REF* we see that the mean
405 July surface melt rate is high (~ 1.5 cm/day) over most of the Arctic basin and is low (< 0.5
406 cm/day) over the Fram Strait, the ice edge and the region of thicker ice north of Greenland
407 and the Canadian Archipelago. Note that the regions of increased surface melt correspond to
408 regions of larger than average pond coverage (not shown). The bottom and lateral melt rates
409 are higher (≥ 1.5 cm/day and ≥ 0.25 cm/day respectively) in regions of low concentration
410 ($A < 80\%$), where solar radiation can penetrate the upper ocean and increase the mixed
411 layer temperature.

412 Figure 5 shows that model runs using the Bitz and Lipscomb (1999) parameterization for
413 salinity and flushing (*NO_MUSHY*, *DBL_ALPHA_H / NO_MUSHY* and *FALSE_BOTTOM*)
414 result in a large increase in surface melt (+0.25 cm/day to +0.5cm/day). This is the result
415 of a slower flushing of melt ponds resulting in a lower surface albedo and higher incoming
416 solar radiation. This in-turn leads to increased heat transfer to the mixed layer and an
417 increase bottom (+0.25 cm/day to +1.0cm/day) and lateral melt rate (up to +0.1 cm/day)
418 over most of the Arctic Ocean. The similarity in the spatial patterns of bottom and lateral
419 melt *DBL_ALPHA_H / NO_MUSHY* and *FALSE_BOTTOM* demonstrates that reducing
420 the heat transfer coefficient only in those location that present large coverage of ponds
421 (pond area larger than 20%) is sufficient to significantly reduce the oceanic melt. This hints
422 to the potentially important role of under ice melt ponds and false bottom formation in
423 controlling the sea ice state.

424 In *LAT_MELT* we observe a large increase of lateral melt over the ice edge (≥ 0.5 cm/day)
425 that is accompanied by a reduction in bottom melt (≤ -0.5 cm/day). This highlights that
426 if more heat is used to melt the ice laterally, less heat is available for bottom melt. Figure
427 5 shows a decrease in *NO_FORM_DRAG* of bottom melt under heavily ridged ice north of
428 Greenland and the Canadian Archipelago (≤ -0.25 cm/day) that we attribute to a reduction

429 in *NO_FORM_DRAG* with respect to *REF* of the oceanic drag coefficient, C_{dw} , and hence
430 a reduction in the heat transfer coefficient, $\alpha_h = C_{dw}/2$.

431 Other interesting spatial features include the near identical spatial patterns of bottom
432 and lateral melt rates in *MLD_CST* and *NO_POND* which mirror the melt rates observed
433 in *MLD_MIN_2M*. We also note that turning off the 3 equation boundary conditions in the
434 *NO_3EQTN* simulation results in an increased bottom and lateral melt in the marginal ice
435 zone. In order to fully understand the pattern of the melt rates discussed above we now look
436 at the impact on the main sea ice and mixed layer characteristics.

437 *b. Regional sea ice and mixed layer patterns*

438 The ice cover is a complex heterogeneous system and in this section we assess how
439 different regions respond to the different physical parameterization schemes. For all model
440 simulations (described in table 1) we calculate for each model grid cell a climatology (over
441 the period 1993 to 2013) of sea ice concentration (A), sea ice thickness (H), ML temperature
442 (T_{mix}) and ML salinity (S_{mix}). As discussed in the introduction, the main focus of this study
443 is in understanding the sensitivity of sea ice melt to various sea ice physics parameterization.
444 Nevertheless, our reference run was chosen to agree qualitatively with ice concentration data
445 obtained from the Special Sensor Microwave Imager (SSM/I) passive microwave radiometer
446 and with ice thickness from the Pan-Arctic Ice Ocean Modeling and Assimilation System
447 (PIOMAS).

448 Comparing h_{mix} from Ice Tethered Profilers (ITP) measurements (2004-2013) and the
449 MYO reanalysis we find that the simulations presented in this study featuring only a simple
450 prognostic ML model reproduce also qualitatively the shallow and stable ML observed across
451 the Arctic (see also Peralta-Ferriz et al. (2014)). In the summer the *REF* simulation and
452 the MYO reanalysis show a shallower ML depth than the ITP measurements, including a
453 minimum depth of $h_{mix} \sim 10$ m over the entire Arctic Ocean. The *REF* simulation ML
454 depths agree with the ITP measurements in the Beaufort Sea but underestimate the ML

455 depths in the pack ice north of Greenland. Similar maps of the mixed layer temperature
456 (T_{mix}) and salinity (S_{mix}) (not shown) illustrate the tendency of the *REF* simulation to
457 overestimate (both against ITP and MYO) the heating of the ML in August, which in turn
458 results in additional melt and a lower S_{mix} .

459 In figures 8 to 11 we show maps of the main sea ice and mixed layer characteristics.
460 We show the absolute values for the reference *REF* simulation and the relative values with
461 respect to *REF* for all other model simulations. We have computed these maps for all months
462 but choose here to only show August. This choice is motivated first by the fact that August
463 has the largest differences between the different sensitivity model runs in our study and also
464 because August sea ice concentration is often underestimated in current sea ice models (Notz
465 2013).

466 Comparing first *REF*, *MLD_CST* and *MLD_MIN_2M* we see that switching off the prog-
467 nostic mixed layer results in a large increase in ice concentration ($A > +10\%$, figure 8) and
468 decrease in the ML temperature ($T_{mix} < -0.4^\circ\text{C}$, figure 10) over most of the eastern Arctic
469 Ocean (where $A < 80\%$, figure 8). Reducing the value of the minimum mixed layer depth
470 (to $h_{mix} = 2$ m) has the opposite effect and results in a large decrease in concentration
471 ($A < -10\%$, figure 8) and increase in the ML temperature ($T_{mix} > +0.4^\circ\text{C}$) over the same
472 region. The impact on ice thickness is more diffuse, with a homogeneous increase in the
473 mean ice thickness (+10cm-25cm, figure 9) over most of the Arctic basin for *MLD_CST* and
474 a corresponding increase in the mixed layer salinity ($> +2$, figure 11). *MLD_MIN_2M* shows
475 a decrease in ice thickness (-50cm to -100cm) over a similar region to *MLD_CST* and a
476 corresponding decrease of the mixed layer salinity (< -2 PSU). This indicates that to a
477 leading order, the ML temperature tends to evolve with sea ice concentration (due to mod-
478 ified incoming solar radiation) while the ML salinity evolves with ice thickness (due to salt
479 exchanges during ice melt/growth). Note that these results hold also in July and throughout
480 the summer season (not shown).

481 We now turn to *REF*, *NO_3EQTN* and *NO_MUSHY* (results for *DBL_ALPHA_H*, *DBL_ALPHA_H*

482 / *NO_3EQTN* and *DBL_ALPHA_H* / *NO_MUSHY* are qualitatively similar) to quantify the
 483 impact of the sea ice salinity dynamics, flushing and three equation boundary condition on
 484 the sea ice and ML. Because of the larger incoming solar radiation associated with the default
 485 halodynamic model of Bitz and Lipscomb (1999) and the default CICE flushing parameter-
 486 ization, sea ice concentration is reduced in *NO_MUSHY* with respect to *REF* by more than
 487 10%, sea ice thickness is reduced by more than 1m, T_{mix} is lower by more than 0.4°C, and
 488 S_{mix} is lower by 0.5 – 1 PSU over most of the Arctic Ocean. Note that *FALSE_BOTTOM*,
 489 the simulation that uses the same Bitz and Lipscomb (1999) parameterization has a similar
 490 low sea ice state bias. Comparing *REF* and *NO_3EQTN*, we see that the differences are
 491 smaller ($\Delta A \sim -5\%$, $\Delta H \sim -20\text{cm}$, $\Delta T_{mix} \sim +0.3^\circ\text{C}$ and $\Delta S_{mix} \sim 0$ PSU), the impact is
 492 localised over the marginal ice zone and happens almost exclusively in the summer season
 493 (June and July not shown). This is consistent with the larger melt rate in this region in
 494 *NO_3EQTN* and reflects the fact the 3 equation boundary condition is most effective where
 495 there is a source of fresh melted water at the ice-ocean interface, hence lowering the inter-
 496 facial salinity, S_0 , and reducing the bottom heat flux (see equations (4) to (6) in section
 497 2b).

498 The impact of switching off the form drag parameterization of Tsamados et al. (2014) in
 499 *NO_FORM_DRAG* is spatially bi-modal; increasing the summer concentration (marginally),
 500 ice thickness ($\Delta H \sim +1\text{m}$) and ML salinity ($\Delta S_{mix} \sim 1$ PSU) in the heavily ridged regions
 501 north of Greenland and the Canadian Archipelago, and decreasing the ice concentration
 502 ($\Delta A \sim -10\%$) and ice thickness ($\Delta H \sim -25\text{cm}$) while increasing the ML temperature
 503 ($\Delta T_{mix} \sim +0.3^\circ\text{C}$) over the Russian continental shelves. As discussed in section 3a, these
 504 differences can be largely explained by increased (reduced) interfacial heat fluxes due to the
 505 higher (lower) than average atmospheric and oceanic heat exchange coefficients in the former
 506 (later) regions when the form drag is accounted for.

507 Switching off the melt ponds in *NO_POND* results, as expected, in a large increase in
 508 the concentration and volume of ice throughout the summer season, due to a lowering of the

509 incoming solar radiation, F_s . In August, for example, the patterns are similar, albeit more
510 intense, to *MLD_CST* with a large increase of A and decrease of T_{mix} over most of the eastern
511 portion of the Arctic Ocean and a more homogeneous increase of S_{mix} and H . Interestingly
512 *FALSE_BOTTOM* performs very much like *NO_MUSHY* (and less like *DBL_ALPHA_H*
513 / *NO_MUSHY*), indicating that reducing the bottom heat flux whenever melt ponds are
514 prevalent could play an important role in accurately simulating the total mass balance of
515 the Arctic sea ice cover.

516 Introducing the new lateral melt parameterization in *LAT_MELT* results in a significant
517 decrease of concentration ($\Delta A \sim -7.5\%$) and thickness ($\Delta H \sim -20\text{cm}$) in the marginal ice
518 zone, but without noticeable changes of the mixed layer salinity and temperature.

519 *c. Impact on the main sea ice characteristics*

520 We now assess the main sea ice characteristics from the various model simulations over
521 the entire Arctic basin. This provides a simple overview of the sea ice response to prescribed
522 atmospheric and oceanic forcing. In figure 12, we look at the impact of the new model
523 physics on the total ice area (figure 12 a-c), total ice extent (figure 12 d-f), and total ice
524 volume (figure 12 g-i). To distinguish between the different model responses shown in figure
525 12 we present in figures 13 (a-c) and 14 (a-c) a series of scatter plots showing the average
526 and trend in sea ice area (SIA), sea ice extent (SIE, defined as the total area covered by ice
527 with a concentration higher than 15%) and sea ice volume (SIV) over the period 1993 to
528 2010 in August and September (note that we use the same colour scheme as in figure 12).
529 The slightly shorter time period chosen reflects the time span of the *SST_TIME* simulation
530 that is limited by the MYO reanalysis data used. Note that the results shown on figures 13
531 and 14 are similar over the period 1993 to 2013.

532 In order to assess the inter-annual variability of the model simulations, we also calculate
533 the correlation and de-trended correlation between each model run annual time-series (SIA,
534 SIE and SIV) and the corresponding observational dataset. Figures 13 (d-f) and 14 (d-f)

535 show these results in a scatter plot format respectively in August and September. Note
 536 that we choose to compare the SIA and SIE results to the Bootstrap processing of passive
 537 microwave data (Comiso 2000). While absolute values between NASA Team and Bootstrap
 538 sea ice concentration vary considerably in the summer, the detrended time series are similar.
 539 For comparison purposes we also show a point corresponding to the Schröder et al. (2014)
 540 model setup that we refer to as *SFFT14*.

541 Figures 13 and 14 reveal that the physical processes tested in this study introduce a wide
 542 spread in the main sea ice characteristics in both the mean and the trend. In September
 543 the average SIA ranges from $3.1 \times 10^6 \text{ km}^2$ (*NO_MUSHY*) to $5.1 \times 10^6 \text{ km}^2$ (*SST_TIME*),
 544 the average SIE from $4.5 \times 10^6 \text{ km}^2$ (*DBL_ALPHA_H / NO_MUSHY*) to $6.2 \times 10^6 \text{ km}^2$
 545 (*SST_TIME*) and the average SIV from $4.0 \times 10^6 \text{ km}^2$ (*DBL_ALPHA_H / NO_MUSHY*) to
 546 $12.7 \times 10^6 \text{ km}^2$ (*SST_TIME*). The September SIA trend ranges from $-1700 \times 10^6 \text{ km}^2/\text{decade}$
 547 (*SST_TIME*) to $-750 \times 10^6 \text{ km}^2/\text{decade}$ (*NO_POND*), the SIE trend ranges from $-1400 \times$
 548 $10^6 \text{ km}^2/\text{decade}$ (*SFFT14*) to $-620 \times 10^6 \text{ km}^2/\text{decade}$ (*MLD_CST*), and the SIV trend
 549 ranges from $-3.9 \times 10^{12} \text{ m}^3$ (*SST_TIME*) to $-1.6 \times 10^{12} \text{ m}^3/\text{decade}$ (*DBL_ALPHA_H /*
 550 *NO_MUSHY*).

551 Looking in more detail at the individual runs in figures 13 a-c and 14 a-c, we see that
 552 the average SIA, SIE and SIV (to a lesser degree) of most model simulations are larger than
 553 for the *SFFT14* simulation of Schröder et al. (2014) and closer to the passive microwave
 554 observations (not closer to PIOMAS). The only simulations that have similar SIA and SIE
 555 (but lower SIV) to the *SFFT14* run are *NO_MUSHY* and *DBL_ALPHA_H / NO_MUSHY*
 556 that use the same thermodynamic treatment of the ice Bitz and Lipscomb (1999) and the
 557 same parameterization of the flushing of melt ponds (Turner and Hunke 2015) as is used in
 558 Schröder et al. (2014). Two outlier runs on figure 12, *NO_MUSHY* (and *DBL_ALPHA_H /*
 559 *NO_MUSHY* not shown) and *SST_TIME* (and to a lesser degree *NO_POND*), show a very
 560 low and high total volume of ice throughout the season (figures 12 (g-i)). In *SST_TIME* we
 561 use a time dependent SST from the MYO reanalysis which is equivalent to modifying the

562 oceanic flux F_{adv} shown on figure 1. As clearly demonstrated in Turner and Hunke (2015),
563 by introducing a new mushy layer thermodynamic scheme (Turner et al. 2013) (*NO_3EQTN*
564 and *REF*), we also modify the flushing parameterization used in the earlier setup of CICE
565 (Bitz and Lipscomb 1999) (*NO_MUSHY*). This results in less melt pond water being flushed
566 in the summer in *NO_MUSHY* as opposed to in *NO_3EQTN* (or *REF*) which lowers the
567 albedo and increases the incoming shortwave radiation penetrating the sea ice and mixed
568 layer system, resulting in a strong reduction in sea ice volume as shown in figures 12 (g-i).
569 This is also highlighted by the additional ice surface heat flux F_s , in *REF* compared to
570 *NO_MUSHY*. Inversely, in *NO_POND* where the thickness and area of the melt ponds are
571 set artificially to zero, the surface heat flux, F_s , is reduced, resulting in less ice melt and a
572 slower ice edge retreat (see figures 12, 13 and 14).

573 Observed differences in the mean sea ice characteristics between the various model sim-
574 ulations can also be related to a shift in their seasonal responses. As highlighted in figure
575 12, introducing a prognostic ML results in an overall depletion of ice across the Arctic (in
576 both thickness and concentration). From figure 12 g (but also a and d) we see that from
577 January to May, the sea ice in the reference run *REF* does grows slower than in *MLD_CST*.
578 We attribute this to the entrainment of warm water from the deeper ocean as the mixed
579 layer deepens from about 30 m in January to about 50 m in May, resulting in a large pos-
580 itive bottom flux F_{bot} (figure 2) that is not present in the *MLD_CST* run. Looking at the
581 mean ice growth and melt contributions in figure 4 and for individual months shows that the
582 difference is due to less frazil ice formation in *REF* between January and May as discussed
583 in section 3a

584 As expected, the trends in SIV correlate with the mean SIV (see figures 13 c and 14
585 c). For example, the ice covered area ice in August in *SST_TIME* is almost double that of
586 *NO_MUSHY* and melting sea ice at the same volume per decade in both runs would require
587 a significant increase in the local melt rates that has no physical justification. Hence, the sea
588 ice volume trend is more than halved in *NO_MUSHY* ($-1.7 \times 10^{12} \text{m}^3/\text{decade}$ in September)

589 in comparison to *SST_TIME* ($-4 \times 10^{12} \text{m}^3/\text{decade}$ in September) as shown in figure 14 c.

590 We turn now to the scatter plot correlations presented in figures 13 d-f and 14 d-f. In the
591 following discussion we denote R the correlation and R^* the detrended correlation. Figure
592 13 d-f shows that apart from *SFFT14* and *SST_TIME*, all other runs perform relatively
593 poorly in reproducing the observed variability in the August SIA ($R \leq 0.75$ and $R^* \leq 0.45$)
594 and only slightly better for the SIE ($R \leq 0.85$ and $R^* \leq 0.6$) and SIV ($R \leq 0.88$ and
595 $R^* \leq 0.63$). The September correlations (figures 14 d-f) are higher in all simulations for SIA
596 ($0.86 \leq R \leq 0.95$ and $0.6 \leq R^* \leq 0.86$) and SIE ($0.82 \leq R \leq 0.95$ and $0.53 \leq R^* \leq 0.86$)
597 and similar for SIV ($0.86 \leq R \leq 0.92$ and $0.45 \leq R^* \leq 0.8$). The *SFFT14* and *SST_TIME*
598 runs still perform best across all characteristics but note that *NO_MUSHY*, *DBL_ALPHA_H*
599 / *NO_MUSHY*, *DBL_ALPHA_H* / *NO_3EQTN*, FD/OFF and *DBL_ALPHA_H* also perform
600 well (in decreasing order) in representing the observed interannual variability of the SIE.

601 Summarising figures 12, 13 and 14 one can conclude that introducing the new physical
602 parameterizations schemes described in section 2 and, in particular, the new mushy-layer
603 thermodynamic approach of Turner et al. (2013) can improve the main basin average char-
604 acteristics of the sea ice with respect to the *SFFT14* setup. The improvement is particularly
605 clear for the August SIA and SIE and the September SIA. However, the potential improve-
606 ment in simulating the sea ice trends is not so clear, where we see an improvement in the
607 August SIE trend but a deterioration of the SIV trends. The inter-annual variability of
608 the main sea ice characteristics quantified by the correlation coefficients, R and R^* , figures
609 13 and 14 show that the model simulations (with the exception of *SST*) do not perform
610 as well as the *SFFT14* simulation. To understand these differences one must realise that
611 inter-annual variability is dependent on the mean state of the ice pack. We expect, for ex-
612 ample, a thinner and less concentrated sea ice cover to be more responsive to interannual
613 variability in the external forcing. This highlights the fact that even within a stand-alone
614 setup, tuning a sea ice model to reproduce simultaneously the mean, trends and interannual
615 variability of the main sea ice characteristics is a delicate exercise. Interestingly we find that

616 the *SST_TIME* simulation outperforms all other model runs in almost every single category
617 both in terms of averages and correlations (note that the *SFFT14* run is better at capturing
618 September SIE interannual variability). While this result is unsurprising in the sense that a
619 time dependent sea surface temperature from reanalysis captures a large part of the inter-
620 annual variability of the atmospheric and oceanic forcing as well as of the sea ice extent,
621 it nevertheless highlights once more the importance of the upper ocean in driving the sea
622 ice response and the coupled nature of the sea ice - mixed layer system (Toole et al. 2010;
623 Perovich et al. 2014).

624 4. Discussion and conclusion

625 We have presented a stand-alone sea ice model sensitivity study focusing on the processes
626 controlling the summer melt of Arctic sea ice. In addition to the parameterization schemes
627 already implemented in the state of the art Los Alamos community sea ice model CICE,
628 v5.0.2 (e.g. explicit melt ponds, a form drag parameterization, and a halodynamic brine
629 drainage scheme) we implement in the model and test three new schemes: i) a prognostic
630 mixed layer model; ii) a three equation boundary condition; and iii) a parameterization
631 of lateral melting explicitly accounting for the average floe size and floe size distribution
632 dependence. For each simulation, the total melt is decomposed into its surface, bottom and
633 lateral melt components. While our modelling approach is limited in that the sea ice model
634 is not coupled to an atmosphere or ocean model preventing a complete representation of
635 feedback processes, it has the advantage that it disentangles model physics uncertainty from
636 the internal variability inherent to a fully coupled model. The reference simulation of this
637 stand-alone sea ice-mixed layer model was still able to simulate accurately the mean state,
638 trends and inter-annual variability of the main Arctic sea ice cover characteristics (ice area,
639 extent and volume).

640 Our sensitivity study demonstrates that the various sea ice parameterization schemes

641 have the potential to significantly impact the sea ice and mixed layer characteristics on
642 regional and basin scales. Introducing a prognostic mixed layer (ML) resulted in an overall
643 decrease of sea ice across the Arctic (in both thickness and concentration). In this simulation,
644 ice growth is reduced due to entrainment of warm water from the deeper ocean as the ML
645 deepens from December to May, while ice growth is enhanced in Autumn due to a more
646 rapid cooling of the shallow ML. Switching off the form drag parameterization increased ice
647 thickness ($\sim +1$ m) over the heavily ridged regions north of Greenland and the Canadian
648 Archipelago and reduced ice thickness (~ -0.25 m) over the Russian continental shelves. We
649 attribute this to the decreased (increased) surface and bottom melt in the former (latter)
650 regions, due to the increased momentum and heat transfer coefficients in these deformed
651 (undeformed) areas. The impact of the 3 equation boundary conditions was localized in
652 the marginal ice zone and acts exclusively during summer, when the temperature difference
653 between the ML and the ice-ocean interface that drives the bottom melt is reduced. The
654 halodynamic brine drainage scheme resulted in a strong reduction in ice thickness (≥ 1 m),
655 due to reduced flushing of melt ponds which lowers the surface albedo and thus results in
656 additional absorption of solar radiation, increasing surface and bottom melt. Conversely,
657 switching off the explicit melt pond scheme resulted in a large increase in sea ice thickness
658 and concentration. Introducing the new parameterization of lateral melt resulted in a large
659 increase in lateral melt over the ice edge that is accompanied by a reduction in bottom melt.
660 Across all simulations, we find that bottom melt accounts typically for around two thirds of
661 the total melt, surface melt accounts for nearly one third and lateral melt accounts for less
662 than 10%.

663 Quantitative optimization of the simulated sea ice and mixed layer against observations
664 was not the primary goal of this study, and is a topic that will be pursued in future work
665 in stand alone and ice-ocean coupled simulations. Nevertheless, this study reveals that such
666 optimization is complex, and will likely require a trade-off between accurately simulating the
667 mean ice state characteristics and capturing the inter-annual ice state variability. The sen-

668 sitivity of the inter-annual variability to different sea ice physics parameterization schemes,
669 alludes to the importance of accurate sea ice physics representation in climate models, espe-
670 cially when seeking skillfull seasonal sea ice forecasts. In particular, the difficulty in current
671 sea ice models to reproduce and forecast years with anomalously high or low sea ice extent
672 (Stroeve et al. 2014) is likely due to deficiencies in the physical representation of sea ice in
673 these models. Moreover, the wide spread in the simulated mean state and trend of the main
674 sea ice characteristics in our sensitivity study indicates that model physics uncertainty could
675 dominate overall sea ice uncertainty in general circulation models (Massonnet et al. 2012).

676 APPENDIX

677 **5. Appendix : Impact of floe size distribution on lateral** 678 **melt**

679 *(iv) Some preliminary equations and definitions*

680 Defining $n_r(r)dr$ as the area fraction covered by ice of size r one has the number of floes
681 of size r per unit area as $\frac{n_r(r)}{\pi r^2}$. To express $n_r(r)$ as a function of the floe area distribution
682 $n_s(s)$ with $s = \pi r^2$ we need the identity:

$$n_s(s) = \frac{n_r(\sqrt{s/\pi})}{2\pi\sqrt{s/\pi}} \quad (5.1)$$

683 From now on we use the simplified notation $n(r)$ instead of $n_r(r)$. We have the condition of
684 normalization for $n(r)$:

$$\int_0^\infty n(r)dr = 1 \quad (5.2)$$

685 For a total surface of ice A we can express the first average floe size \bar{r}_1 as:

$$\bar{r} = \int_0^\infty A \frac{n(r)}{\pi r^2} r dr / \int_0^\infty S \frac{n(r)}{\pi r^2} dr. \quad (5.3)$$

686 Note that $\int_0^\infty A \frac{n(r)}{\pi r^2} dr$ is the total number of floes in that area S . Lets choose 2 function $n(r)$
 687 one for a fixed floe size case ($n_1(r)$) and one for a power law FSD ($n_2(r)$). We also assume
 688 that both have the same average floe size \bar{r} . For the fixed floe size case, the normalization
 689 equation (5.2) is satisfied for $n_1(r) = \delta(r - \bar{r})$. The normalization equation for $n_2(r)$ gives:

$$\int_0^\infty n_2(r) dr = \int_0^\infty C r^{-\zeta} dr = \int_{r_{min}}^\infty C r^{-\zeta} dr = C \frac{r_{min}^{-\zeta+1}}{\zeta - 1} = 1. \quad (5.4)$$

690 Therefore one can write:

$$n_2(r) = (\zeta - 1) r^{-\zeta} r_{min}^{\zeta-1}. \quad (5.5)$$

691 Now the condition (5.3) can be written:

$$\int_0^\infty A \frac{n_2(r)}{\pi r^2} r dr / \int_0^\infty A \frac{n_2(r)}{\pi r^2} dr = \int_0^\infty r^{-\zeta-1} / \int_0^\infty r^{-\zeta-2} = \frac{\zeta + 1}{\zeta} r_{min} = \bar{r}. \quad (5.6)$$

692 And we can write r_{min} as a function of \bar{r} .

693 *(v) On why power law FSD melt less ice laterally than fixed floe size.*

694 We know that the rate of lateral melting of the total ice area is proportional to the total
 695 perimeter P of the floes:

$$\frac{\partial A}{\partial t} = -mP = -m \frac{P}{A} A, \quad (5.7)$$

696 where m is the lateral rate of melt (in cm/s). Lets calculate this perimeter for the two
 697 situations described above. Note both have the same average floe size \bar{r} . We have

$$P_1 = 2A \frac{1}{\bar{r}}, \quad (5.8)$$

698 and

$$P_2 = A \int_0^\infty \frac{n_2(r)}{\pi r^2} 2\pi r dr = 2A \frac{(\zeta - 1)(\zeta + 1)}{\zeta^2} \frac{1}{\bar{r}} = 2P_0(\zeta)A \frac{1}{\bar{r}}. \quad (5.9)$$

699 Typical observed values of ζ are in the range 0 to 2. But the total area of ice diverges if
700 $\zeta < 1$ and one needs to introduce a upper floe size cutoff value. Example values in this range
701 for the function P_0 are $P_0(2.0) = 0.75$, $P_0(1.75) = 0.67$, $P_0(1.5) = 0.56$, $P_0(1.25) = 0.36$,
702 $P_0(1.1) = 0.17$ and $P_0(1.0) = 0$. Herman 2010 introduces a different function P_0 that takes
703 the values $P_0(2.0) = 1$, $P_0(1.75) = 0.86$, $P_0(1.5) = 0.67$, $P_0(1.25) = 0.4$, $P_0(1.1) = 0.18$ and
704 $P_0(1.0+) = 0$

705 We would like to acknowledge the Natural Environment Research Council for supporting
706 this work.

707 NCEP Reanalysis 2 data were provided by the NOAA NationalWeather Service, USA,
708 from their website at http://nomads.ncep.noaa.gov/txt_descriptions/servers.shtml.

709

710 REFERENCES

711 Bitz, C. and W. Lipscomb, 1999: An energy-conserving thermodynamic model of sea ice.
712 *Journal of Geophysical Research*, **104 (15)**, 669–15.

713 Bitz, C. M., P. R. Gent, R. A. Woodgate, M. M. Holland, and R. Lindsay, 2006: The
714 influence of sea ice on ocean heat uptake in response to increasing CO₂. *J. Climate*,
715 **19 (11)**, 2437–2450.

716 Briegleb, B. and B. Light, 2007: A delta-eddington multiple scattering parameterization for
717 solar radiation in the sea ice component of the community climate system model. near

718 tech. Tech. rep., Note NCAR/TN-472+ STR, National Center for Atmospheric Research,
719 2007.

720 Comiso, J. C., 2000, updated 2014: Bootstrap sea ice concentrations from Nimbus-7 SMMR
721 and DMSP SSM/I-SSMIS Version 2 [1980-2013], Boulder, Colorado USA: NASA DAAC
722 at the National Snow and Ice Data Center..

723 Comiso, J. C., 2011: Large Decadal Decline of the Arctic Multiyear Ice Cover. *J. Climate*,
724 **25**, 1176–1193.

725 Coon, M., R. Kwok, G. Levy, M. Pruis, H. Schreyer, and D. Sulsky, 2007: Arctic ice dy-
726 namics joint experiment (aidjex) assumptions revisited and found inadequate. *Journal of*
727 *Geophysical Research-Oceans*, **112 (C11)**, C11S90.

728 Ebert, E. E. and J. A. Curry, 1993: An intermediate one-dimensional thermodynamic sea ice
729 model for investigating ice-atmosphere interactions. *J. Geophys. Res.*, **98 (C6)**, 10 085–
730 10 109.

731 Feltham, D. , 2008: Sea ice rheology. *Annual Review of Fluid Mechanics*

732 Feltham, D. L., N. Untersteiner, J. S. Wettlaufer, and M. G. Worster, 2006: Sea ice is a
733 mushy layer. *Geophys. Res. Lett.*, **40**, 91–112.

734 Ferry, N., S. Masina, A. Storto, K. Haines, M. Valdivieso, B. Barnier, and J.-M. Molines,
735 2011: Product user manual global-reanalysis-phys-001-004-a and b, myocean. Tech. rep.

736 Flocco, D., D. Schroeder, D. L. Feltham, and E. C. Hunke, 2012: Impact of melt ponds on
737 arctic sea ice simulations from 1990 to 2007. *J. Geophys. Res.*, **117 (C9)**, C09 032–.

738 Herman, A., 2010: Sea-ice floe-size distribution in the context of spontaneous scaling emer-
739 gence in stochastic systems. *Phys. Rev. E*, **81 (6)**, 066 123–.

740 Hibler, W., J. Hutchings, and C. Ip, 2006: Sea-ice arching and multiple flow states of arctic
741 pack ice. *Annals of Glaciology*, **44 (1)**, 339–344.

742 Hunke, E. and J. Dukowicz, 2002: The elastic-viscous-plastic sea ice dynamics model in
743 general orthogonal curvilinear coordinates on a sphere - incorporation of metric terms.
744 *Monthly weather review*.

745 Hunke, E. C., 2014: Weighing the importance of surface forcing on sea ice - a september
746 2007 modeling study. *Q.J.R. Meteorol. Soc.*, n/a–n/a.

747 Hunke, E. C., D. A. Hebert, and O. Lecomte, 2013: Level-ice melt ponds in the los alamos
748 sea ice model, cice. *Ocean Modelling*, **71 (0)**, 26–42.

749 Hunke, E. C., W. H. Lipscomb, A. K. Turner, N. Jeffery, and S. Elliott, 2013: CICE: the
750 Los Alamos Sea Ice Model Documentation and Software User’s Manual Version 5.0.

751 Johnson, M., S. Gaffigan, E. Hunke, and R. Gerdes, 2007: A comparison of arctic ocean sea
752 ice concentration among the coordinated aomip model experiments. *Journal of Geophysical*
753 *Research: Oceans (1978–2012)*, **112 (C4)**.

754 Kanamitsu, M. , Ebisuzaki, W. , Woollen, J. , Yang, S. , Hnilo, J. J., Fiorino, M. and
755 Potter, G. L., 2002: NCEP-DOE AMIP-II Reanalysis (R-2). *Bull. Amer. Meteor. Soc.*,
756 **83** 1631–1643.

757 Keen, A. B., H. T. Hewitt, J. K. Ridley, 2013: A case study of a modelled episode of low
758 Arctic sea ice. *Clim. Dyn.*, **41** 1229–1244.

759 Kwok, R. and D. A. Rothrock, 2009: Decline in Arctic sea ice thickness from submarine and
760 ICESat records: 1958–2008. *Geophys. Res. Lett.*, 2009GL036 L15501–.

761 Kraus, E. B. and J. S. Turner, 1967: A one-dimensional model of the seasonal thermocline
762 ii. the general theory and its consequences. *Tellus*, **19 (1)**, 98–106.

763 Laxon, S. W., L. A. Giles, A. L. Ridout, D. J. Wingham, Duncan J. R. Willatt, R. Cullen,
764 R. Kwok, A. Schweiger, J. Zhang, C. Haas, Christian S. Hendricks, R. Krishfield, N. Kurtz,

765 Nathan, S. Farrell, M. Davidson, 2013: CryoSat-2 estimates of Arctic sea ice thickness
766 and volume. *Geophys. Res. Lett.*, 2013GL036.

767 Lindsay R. and A. Schweiger, 2013: Arctic sea ice thickness loss determined using subsur-
768 face, aircraft, and satellite observations. *The Cryosphere*, **9**, 269–283.

769 Lipscomb, W. and E. Hunke, 2004: Modeling sea ice transport using incremental remapping.
770 *Monthly Weather Review*, **132 (6)**, 1341–1354.

771 Lipscomb, W., E. Hunke, W. Maslowski, and J. Jakacki, 2007: Ridging, strength, and
772 stability in high-resolution sea ice models. *J. Geophys. Res.*, **112**.

773 Lu, P., Z. Li, B. Cheng, and M. Leppäranta, 2011: A parameterization of the ice-ocean drag
774 coefficient. *J. Geophys. Res.*, **116 (C7)**, C07019–.

775 Lüpkes, C., V. M. Gryanik, J. Hartmann, and E. L. Andreas, 2012: A parametrization, based
776 on sea ice morphology, of the neutral atmospheric drag coefficients for weather prediction
777 and climate models. *J. Geophys. Res.*, **117 (D13)**, D13112–.

778 Maslowski, W., J. Clement Kinney, M. Higgins, and A. Roberts, 2012: The future of arctic
779 sea ice. *Annu. Rev. Earth Planet. Sci.*, **40 (1)**, 625–654.

780 Massonnet, F., T. Fichefet, H. Goosse, C. M. Bitz, G. Philippon-Berthier, M. M. Holland,
781 and P.-Y. Barriat, 2012: Constraining projections of summer arctic sea ice. *The Cryosphere*
782 *Discussions*, **6 (4)**, 2931–2959.

783 Maykut, G. A. and M. G. McPhee, 1995: Solar heating of the arctic mixed layer. *J. Geophys.*
784 *Res.*, **100 (C12)**, 24691–24703.

785 Maykut, G. A. and D. K. Perovich, 1987: The role of shortwave radiation in the summer
786 decay of a sea ice cover. *J. Geophys. Res.*, **92 (C7)**.

- 787 McPhee, M. G., 2008: Physics of early summer ice/ocean exchanges in the western weddell
788 sea during ispol. *Deep Sea Research Part II: Topical Studies in Oceanography*, **55**, 1075–
789 1097.
- 790 McPhee, M. G., 2012: Advances in understanding ice–ocean stress during and since aidjex.
791 *Cold Regions Science and Technology*, **76**, 24–36.
- 792 Notz, D., 2005: Thermodynamic and fluid-dynamical processes in sea ice. Ph.D. thesis,
793 University of Cambridge.
- 794 Notz, D., 2012: Challenges in simulating sea ice in earth system models. *WIREs Clim*
795 *Change*, **3** (6), 509–526.
- 796 Notz D. , 2013: Sea-ice extent provides a limited metric of model performance. *The*
797 *Cryosphere*, **7**, 3095–3131.
- 798 Overland, J. E. and M. Wang, 2013: When will the summer arctic be nearly sea ice free?
799 *Geophys. Res. Lett.*, **40** (10), 20972101.
- 800 Peralta-Ferriz, C. and R.A.. Woodgate, 2014: Seasonal and interannual variability of pan-
801 Arctic surface mixed layer properties from 1979 to 2012 from hydrographic data, and the
802 dominance of stratification for multiyear mixed layer depth shoaling. *Progress in Oceanog-*
803 *raphy*.
- 804 Perovich, D., J. Richter-Menge, C. Polashenski, B. Elder, T. Arbetter, and O. Brennick,
805 2014: Sea ice mass balance observations from the north pole environmental observatory.
806 *Geophys. Res. Lett.*, 2014GL059356–.
- 807 Perovich, D. K., 1983: On the summer decay of a sea ice cover. Ph.D. thesis, University of
808 Washington.
- 809 Petty, A. A., D. L. Feltham, and P. R. Holland, 2012: Impact of atmospheric forcing on
810 antarctic continental shelf water masses. *J. Phys. Oceanogr.*, **43** (5), 920–940.

- 811 Petty, A. A., P. R. Holland, and D. L. Feltham, 2014: Sea ice and the ocean mixed layer
812 over the antarctic shelf seas. *The Cryosphere*, **8** (2), 761–783.
- 813 Rae, J.G. L., H. T. Hewitt, A. B. Keen, J. K. Ridley, J. M. Edwards, C. M. Harris, 2014: A
814 sensitivity study of the sea ice simulation in the global coupled climate model, HadGEM3
815 . *Ocean Modelling*, **74**, 60–76.
- 816 Rampal, P., J. Weiss, D. Marsan, and M. Bourgoïn, 2009: Arctic sea ice velocity field:
817 General circulation and turbulent-like fluctuations. *J. Geophys. Res.*, **114**, C10014–.
- 818 Rampal, P., J. Weiss, C. Dubois, and J.-M. Campin, 2011: Ipcc climate models do not cap-
819 ture arctic sea ice drift acceleration: Consequences in terms of projected sea ice thinning
820 and decline. *J. Geophys. Res.*, **116**, C00D07–.
- 821 Richter-Menge, J.A., D.K. Perovich, C. Dubois, B.C. Elder, K. Claffey, I. Rigor, and M.
822 Ortmeier, 2011: Ice mass-balance buoys: a tool for measuring and attributing changes in
823 the thickness of the Arctic sea-ice cover. *Annals of Glaciology*, **44** (1), 205–210.
- 824 Rothrock, D., 1975: The energetics of the plastic deformation of pack ice by ridging. *Journal*
825 *of Geophysical Research-Oceans*, **80** (33).
- 826 Schmidt, G. A., C. M. Bitz, U. Mikolajewicz, and L.-B. Tremblay, 2004: Ice-ocean boundary
827 conditions for coupled models. *Ocean Modelling*, **7** (1??2), 59–74.
- 828 Schröder, D., D. L. Feltham, D. Flocco, and M. Tsamados, 2014: September arctic sea-ice
829 minimum predicted by spring melt-pond fraction. *Nature Clim. Change*, **4** (5), 353–357.
- 830 Schröder, D., T. Vihma, A. Kerber, and B. Brmmer, 2003: On the parameterization of
831 turbulent surface fluxes over heterogeneous sea ice surfaces. *J. Geophys. Res.*, **108** (C6),
832 3195–.
- 833 Spreen, G., R. Kwok, and D. Menemenlis, 2011: Trends in Arctic sea ice drift and role of
834 wind forcing: 1992-2009. *Geophys. Res. Lett.*, 2011GL038 L19501–.

835 Steele, M., 1992: Sea ice melting and floe geometry in a simple ice-ocean model. *J. Geophys.*
836 *Res.*, **97 (C11)**, 17 729–17 738.

837 Steele, M., J. H. Morison, and N. Untersteiner, 1989: The partition of air-ice-ocean momen-
838 tum exchange as a function of ice concentration, roe size, and draft. *J. Geophys. Res.*,
839 **94 (C9)**, 12 739–12 750.

840 Steele, M., J. Zhang, and W. Ermold, 2010: Mechanisms of summertime upper arctic ocean
841 warming and the effect on sea ice melt. *J. Geophys. Res.*, **115 (C11)**, C11 004–.

842 Stroeve, J., L. C., V. Kattsov and A. Barrett, M. Serreze, T. Pavlova, M. Holland,
843 W. N.Meier, 2012: Trends in Arctic sea ice extent from CMIP5, CMIP3 and observa-
844 tions. *Geophys. Res. Lett.*, 2012GL039 L16502–.

845 Stroeve, J., L. C. Hamilton, C. M. Bitz, and E. Blanchard-Wrigglesworth, 2014: Predicting
846 september sea ice ensemble skill of the search sea ice outlook 2008-2013. *Geophys. Res.*
847 *Lett.*, 2014GL059 388–.

848 Strong, C. and I. G. Rigor, 2013: Arctic marginal ice zone trending wider in summer and
849 narrower in winter. *Geophys. Res. Lett.*, 2013GL040 4864–4868.

850 Toole, J. M., M.-L. Timmermans, D. K. Perovich, R. A. Krishfield, A. Proshutinsky, and
851 J. Richter-Menge, 2010: Influences of the ocean surface mixed layer and thermohaline
852 stratification on arctic sea ice in the central canada basin. *Journal of Geophysical Research:*
853 *Oceans (1978–2012)*, **115 (C10)**

854 Toole, J. M., R. A. Krishfield, M.-L. Timmermans, and A. Proshutinsky, 2011: The Ice-
855 Tethered Profiler: Argo of the Arctic. *Oceanography (1978–2012)*, **24 (3)**, 126–135.

856 Tsamados, M., D. L. Feltham, D. Schroeder, D. Flocco, S. L. Farrell, N. Kurtz, S. W. Laxon,
857 and S. Bacon, 2014: Impact of variable atmospheric and oceanic form drag on simulations
858 of arctic sea ice*. *J. Phys. Oceanogr.*, **44 (5)**, 1329–1353.

- 859 Tsamados, M., D. L. Feltham, and A. V. Wilchinsky, 2013: Impact of a new anisotropic rhe-
860 ology on simulations of arctic sea ice. *Journal of Geophysical Research: Oceans*, **118** (1),
861 91–107.
- 862 Turner, A. K. and E. Hunke, 2015: Impacts of a mushy-layer thermodynamic approach in
863 global sea-ice simulations using the cice sea-ice model. *Journal of Geophysical Research:*
864 *Oceans*, **120** (2), 1253–1275.
- 865 Turner, A. K., E. C. Hunke, and C. M. Bitz, 2013: Two modes of sea-ice gravity drainage: A
866 parameterization for large-scale modeling. *J. Geophys. Res. Oceans*, **118** (5), 2279–2294.
- 867 Weiss, J. and D. Marsan, 2004: Scale properties of sea ice deformation and fracturing.
868 *Comptes rendus-Physique*, **5** (7), 735–751.
- 869 Williams, T. D., L. G. Bennets, V. A. Squire, D. Dumont, and L. Bertino, 2013: Wave-ice
870 interactions in the marginal ice zone. Part 1: Theoretical foundations. *Ocean Modelling*,
871 **71** (0), 81–91.

872 **6. Figures & Tables**

Description	Name
REF	Reference run: prognostic ML (Petty et al. 2014) ^a ; low heat transfer coefficient $\alpha_h = C_{dw}/2$, form drag (Tsamados et al. 2014), fixed floe size ($L = 300\text{m}$), thermodynamics and flushing of Turner and Hunke (2015) ^a ; 3 equation boundary condition ^c
MLD_CST	As <i>REF</i> but default prescribed ML ($h_{mix} = 20\text{m}$) ^b
MLD_MIN_2M	As <i>REF</i> but $h_{mix}^{min} = 2\text{m}$ instead of default $h_{mix}^{min} = 10\text{m}$ ^a
NO_3EQTN	As <i>REF</i> but default boundary condition $T_0 = T_f(S_{mix})$ ^c
NO_MUSHY	As <i>REF</i> but thermodynamics of Bitz and Lipscomb (1999) and default boundary condition $T_0 = T_f(S_{mix})$ ^c
DBL_ALPHA_H	As <i>REF</i> but $\alpha_h = C_{dw}$ ^c
DBL_ALPHA_H	
/ NO_3EQTN	As <i>REF</i> but doubling heat transfer coefficient $\alpha_h = C_{dw}$ and default boundary condition $T_0 = T_f(S_{mix})$ ^c
DBL_ALPHA_H	
/ NO_MUSHY	As <i>REF</i> but doubling heat transfer coefficient $\alpha_h = C_{dw}$, thermodynamics of Bitz and Lipscomb (1999), and default boundary condition $T_0 = T_f(S_{mix})$ ^c
NO_POND	As <i>REF</i> but melt ponds area and thickness set to zero ^d
FALSE_BOTTOM	As <i>REF</i> but Thermodynamics of Bitz and Lipscomb (1999), $T_0 = T_f(S_{mix})$ ^c ; $\alpha_h = C_{dw}$ but $\alpha_h = C_{dw}/2$ if $A_p \geq 20\%$ in ad-hoc description of false bottoms ^d
NO_FORM_DRAG	As <i>REF</i> but $C_{da} = 1.2 \times 10^{-3}$, $C_{dw} = 6.09 \times 10^{-3}$ SKIN setup of Tsamados et al. (2014) ^e
LAT_MELT	As <i>REF</i> but Power law FSD with average floe size $L(A)$, ^f
SST_TIME	As <i>REF</i> but Temperature restoring towards a time dependent MYO SST ^a
SFFT14	Setup of Schröder et al. (2014) (fixed ML depth, $\alpha_h = 0.006$).

^a See section 2i. All other model runs contain a single modification with respect to REF.

^b See section 2a.

^c See section 2iii, note that BF stands here for bottom flux.

^d See section 2a, note that FB stands here for false bottom.

873 List of Figures

- 874 1 Schematic of the new prognostic ML module and of the other main thermo-
875 dynamic processes included in CICE. The main heat fluxes are highlighted in
876 red while the main salt and freshwater fluxes are shown in black. Adapted
877 from Petty et al. (2014). 41
- 878 2 Climatology of the seasonal cycle of main components of the heat budget of
879 the Arctic sea ice (a) and ML (b) over the period 1993 to 2012. All terms are
880 expressed as an equivalent amount of heat entering the ice or ML (in Joules). 42
- 881 3 Impact of the sensitivity model runs on sea surface temperature (a)-(b), sea
882 surface salinity (e)-(f), ML depth (i)-(j), top melt (c)-(d), bottom melt (g)-
883 (h) and lateral melt (k)-(l). Figures on the first and third columns show the
884 seasonal climatology calculated over the period 1993 to 2012 while columns
885 two and four show time series for July (except (j) that shows the MLD in
886 March). The colour code is the same as in figure 2. 43
- 887 4 Mean annual volume of ice gained or lost through thermodynamic processes
888 associated with our collection of models between 1993 and 2010. The incre-
889 mental differences from the reference run *REF* volume for each process are
890 shown in the second plot; e.g., positive melt terms indicate increased ice vol-
891 ume due to decreased melting, relative to *REF*. Notice the differing scales in
892 the two plots. 44
- 893 5 Maps of the climatology of the average July top melt over the period 1994 to
894 2013 for all sensitivity runs. Note that the map for the *REF* model run is given
895 in absolute melt rate values (in cm/day, top color bar) while all other model
896 runs are given as difference in melt rate with respect to *REF* (in cm/day,
897 bottom color bar). 45

- 898 6 Maps of the climatology of the average July bottom melt over the period
899 1994 to 2013 for all sensitivity runs. Note that the map for the *REF* model
900 run is given in absolute melt rate values (in cm/day, top color bar) while all
901 other model runs are given as difference in melt rate with respect to *REF* (in
902 cm/day, bottom color bar). 46
- 903 7 Maps of the climatology of the average July lateral melt over the period 1994
904 to 2013 for all sensitivity runs. Note that the map for the *REF* model run
905 is given in absolute melt rate values (in cm/day, top color bar) while all
906 other model runs are given as difference in melt rate with respect to *REF* (in
907 cm/day, bottom color bar). 47
- 908 8 August sea ice concentration climatology maps over the period 1994 to 2013
909 for all sensitivity runs. Note that the map for the *REF* model run is given in
910 absolute concentration values (in %, top color bar) while all other model runs
911 are given as difference in concentration with respect to *REF* (in %, bottom
912 color bar). 48
- 913 9 August sea ice thickness climatology maps over the period 1994 to 2013 for
914 all sensitivity runs. Note that the map for the *REF* model run is given in
915 absolute thickness values (metres, in top color bar) while all other model runs
916 are given as difference in thickness with respect to *REF* (metres, in bottom
917 color bar). 49
- 918 10 August mixed layer temperature climatology maps over the period 1994 to
919 2013 for all sensitivity runs. Note that the map for the *REF* model run is
920 given in absolute temperature values ($^{\circ}\text{C}$, in top color bar) while all other
921 model runs are given in as difference in temperature with respect to *REF*
922 ($^{\circ}\text{C}$, bottom color bar). 50

- 923 11 August mixed layer salinity climatology maps over the period 1994 to 2013
924 for all sensitivity runs. Note that the map for the *REF* model run is given in
925 absolute salinity values (PSU, top color bar) while all other model runs are
926 given as difference in salinity with respect to *REF* (PSU, bottom color bar). 51
- 927 12 Impact of the sensitivity model runs on the total area (a)-(c), total extent (d)-
928 (f) and total volume (g)-(i) of sea ice. Figures on the first column show the sea-
929 sonal climatology calculated over the period 1993 to 2012 while columns two
930 and three show the time series for August and September. The colour code is a
931 follows: *REF* in red, *MLD_CST* in blue, *SST_TIME* in green, *MLD_MIN_2M*
932 in mauve, *SSMINT* and *PIOMAS* in solid black and *SSMIBT* in dashed
933 black. 52
- 934 13 Scatter plots of the trends vs averages over the period 1993 to 2010 of the
935 August total sea ice area (a), sea ice extent (b) and sea ice volume (c). Scatter
936 plots of the full and de-trended correlation coefficients between the model and
937 observed time series of the total sea ice area (d), sea ice extent (d) and sea
938 ice volume (f). Here we correlate model sea ice area and extent with the
939 *SSMIBT* observation and model volume with *PIOMAS*. We show 13 model
940 runs described in section 2. As a reference we also show values from the model
941 run discussed in Schröder et al. (2014). 53
- 942 14 Scatter plots of the trends vs averages over the period 1993 to 2010 of the
943 September total sea ice area (a), sea ice extent (b) and sea ice volume (c).
944 Scatter plots of the full and de-trended correlation coefficients between the
945 model and observed time series of the total sea ice area (d), sea ice extent
946 (e) and sea ice volume (f). Here we correlate model sea ice area and extent
947 with the *SSMIBT* observation and model volume with *PIOMAS*. We show
948 13 model runs described in section 2. As a reference we also show values from
949 the model run discussed in Schröder et al. (2014). 54

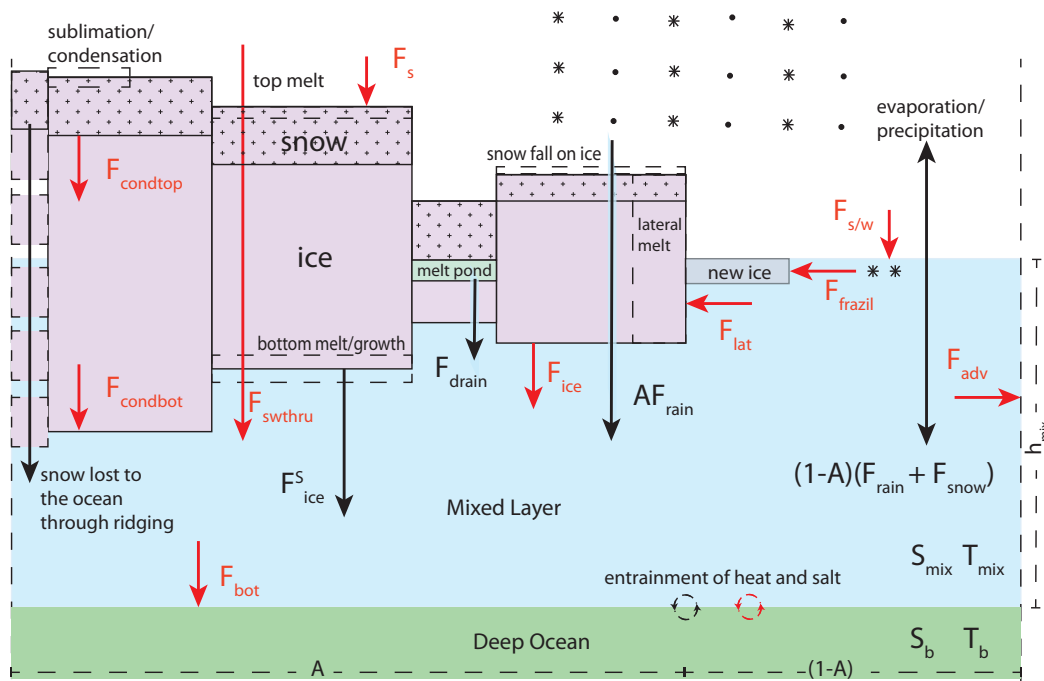


FIG. 1. Schematic of the new prognostic ML module and of the other main thermodynamic processes included in CICE. The main heat fluxes are highlighted in red while the main salt and freshwater fluxes are shown in black. Adapted from Petty et al. (2014).

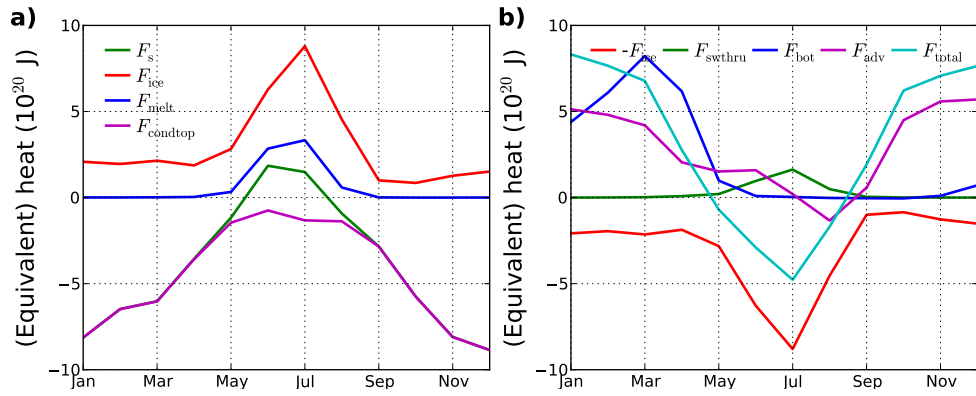


FIG. 2. Climatology of the seasonal cycle of main components of the heat budget of the Arctic sea ice (a) and ML (b) over the period 1993 to 2012. All terms are expressed as an equivalent amount of heat entering the ice or ML (in Joules).

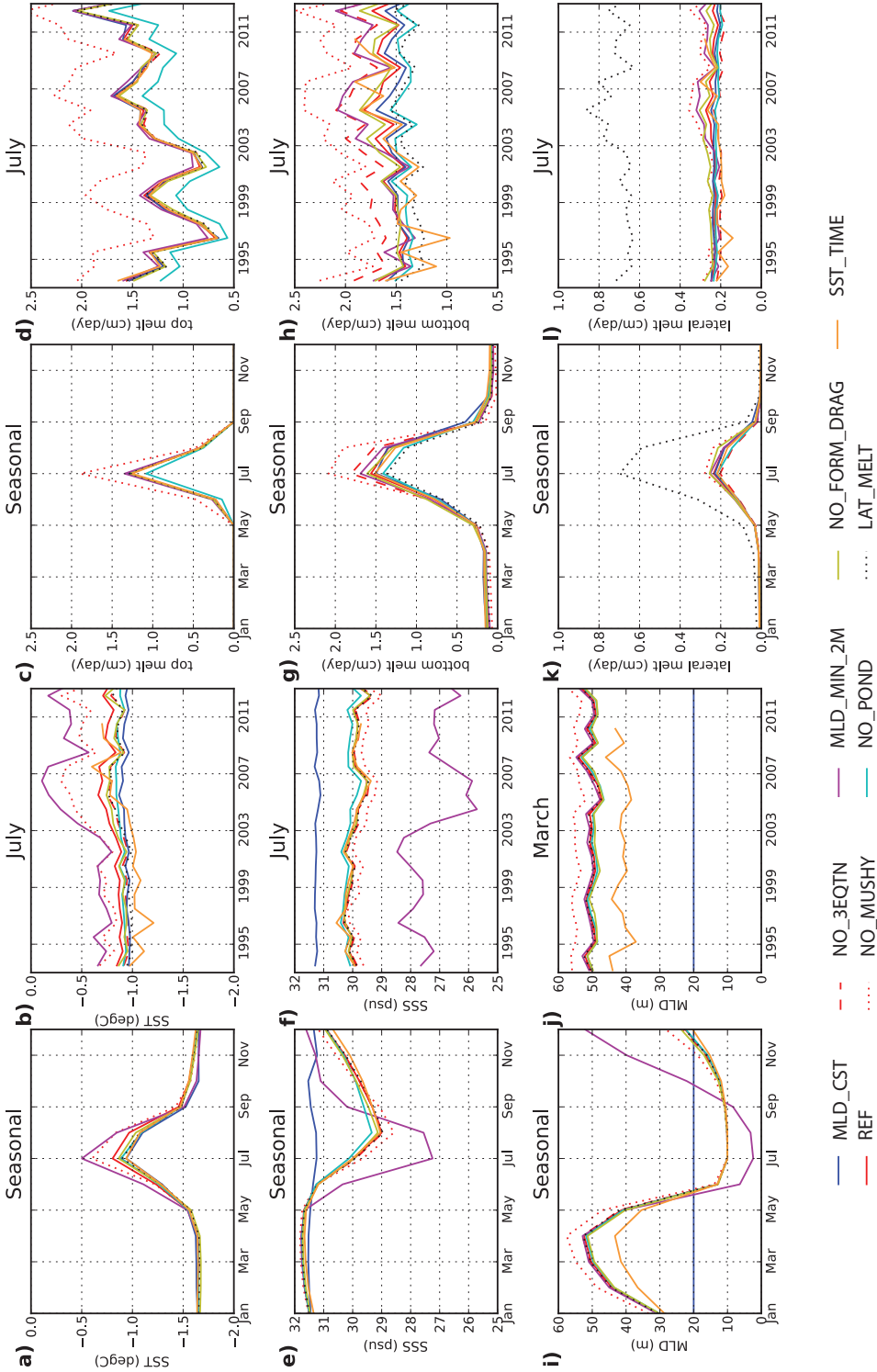


FIG. 3. Impact of the sensitivity model runs on sea surface temperature (a)-(b), sea surface salinity (e)-(f), ML depth (i)-(j), top melt (c)-(d), bottom melt (g)-(h) and lateral melt (k)-(l). Figures on the first and third columns show the seasonal climatology calculated over the period 1993 to 2012 while columns two and four show time series for July (except (j) that shows the MLD in March). The colour code is the same as in figure 2.

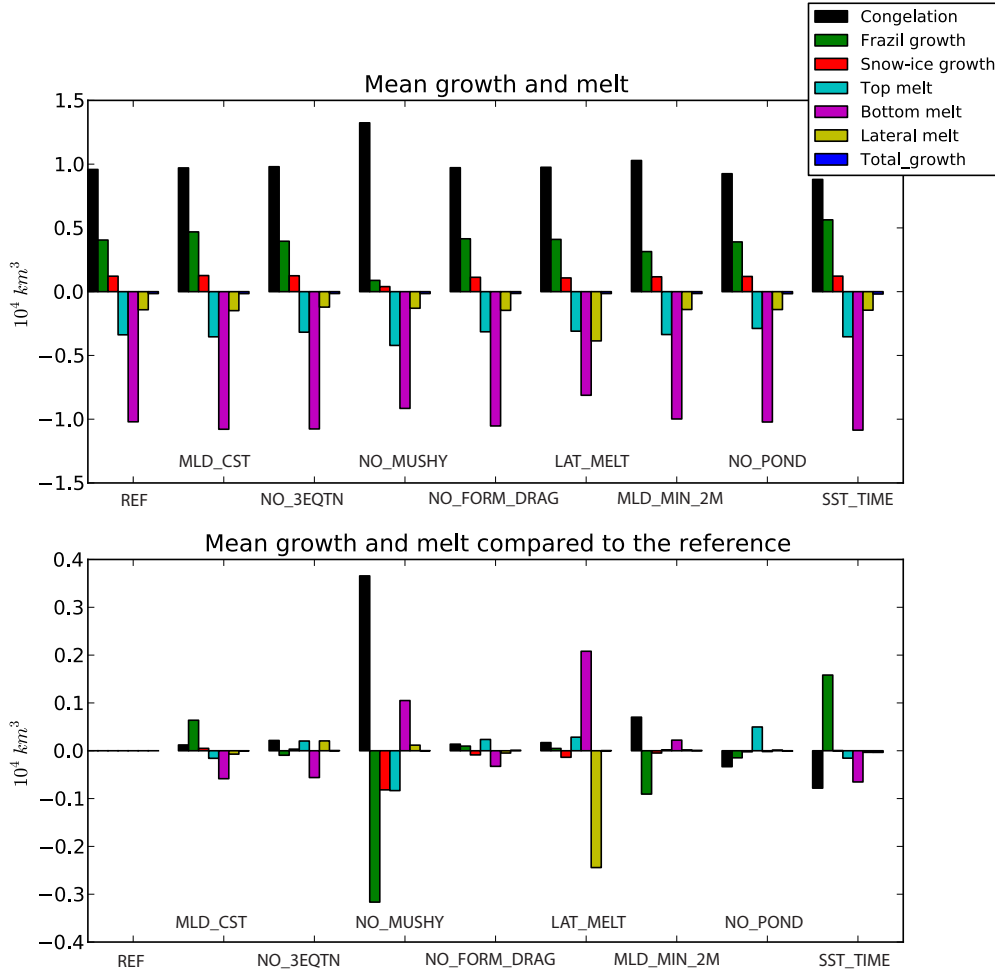


FIG. 4. Mean annual volume of ice gained or lost through thermodynamic processes associated with our collection of models between 1993 and 2010. The incremental differences from the reference run *REF* volume for each process are shown in the second plot; e.g., positive melt terms indicate increased ice volume due to decreased melting, relative to REF. Notice the differing scales in the two plots.

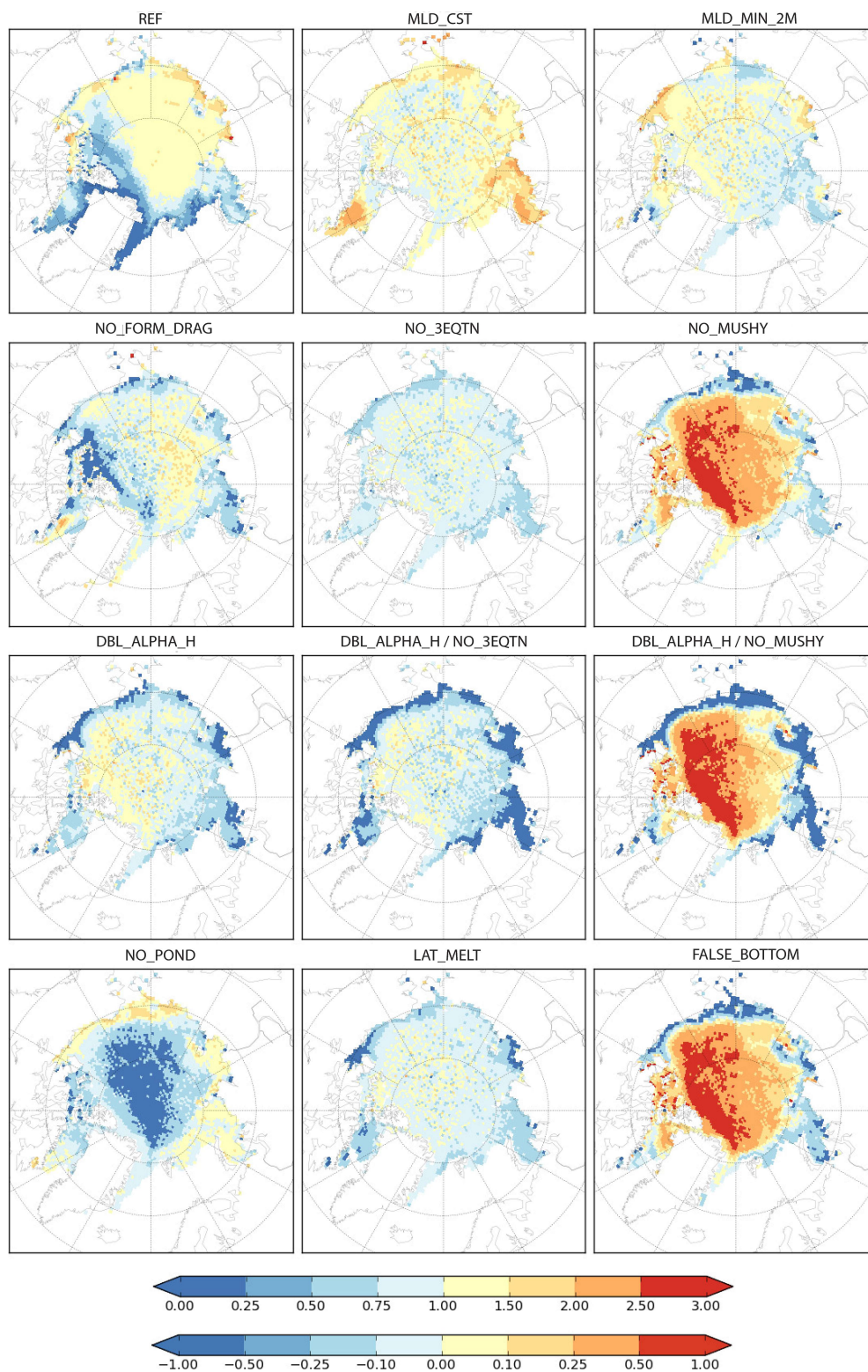


FIG. 5. Maps of the climatology of the average July top melt over the period 1994 to 2013 for all sensitivity runs. Note that the map for the *REF* model run is given in absolute melt rate values (in cm/day, top color bar) while all other model runs are given as difference in melt rate with respect to *REF* (in cm/day, bottom color bar).

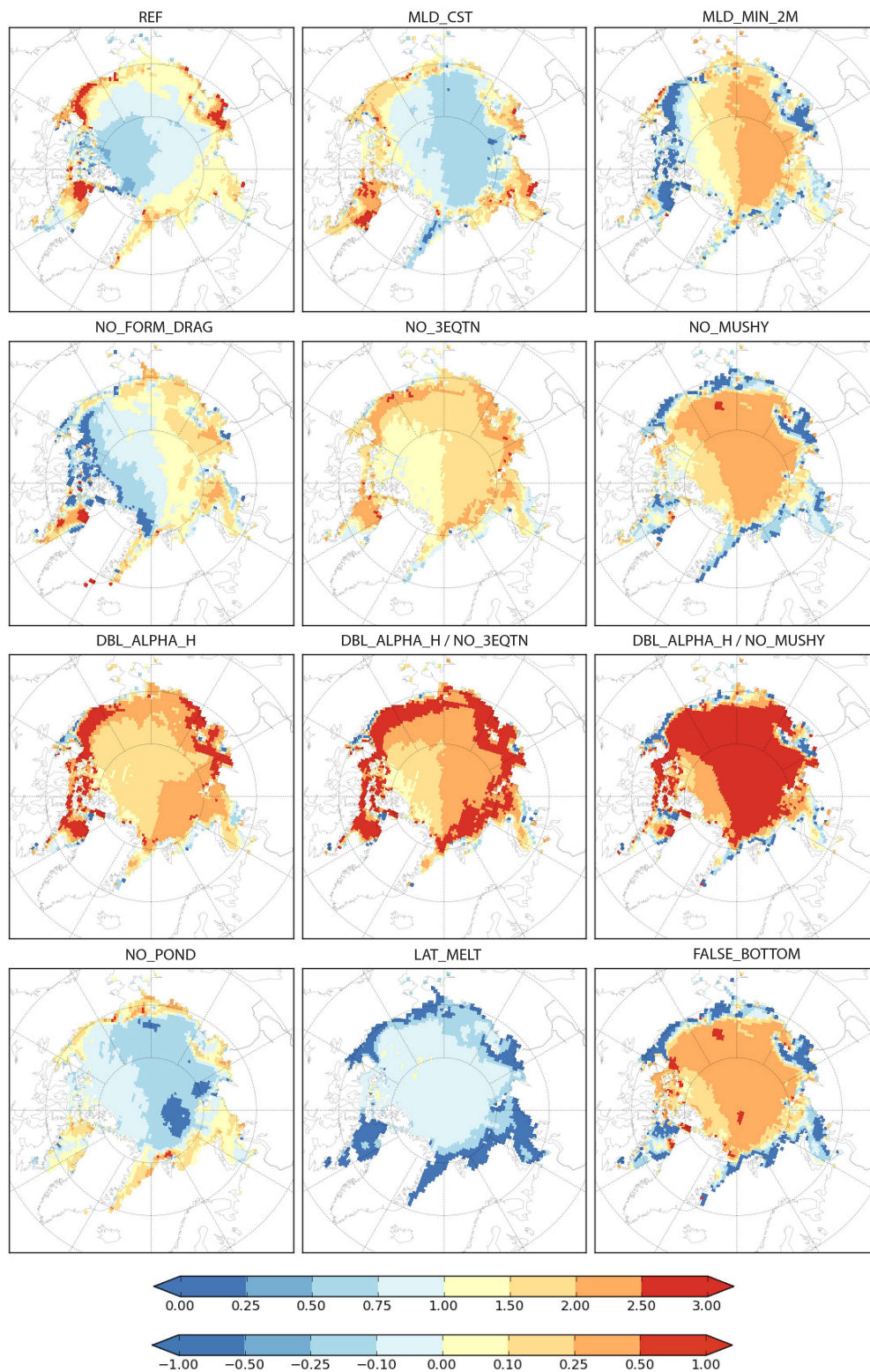


FIG. 6. Maps of the climatology of the average July bottom melt over the period 1994 to 2013 for all sensitivity runs. Note that the map for the *REF* model run is given in absolute melt rate values (in cm/day, top color bar) while all other model runs are given as difference in melt rate with respect to *REF* (in cm/day, bottom color bar).

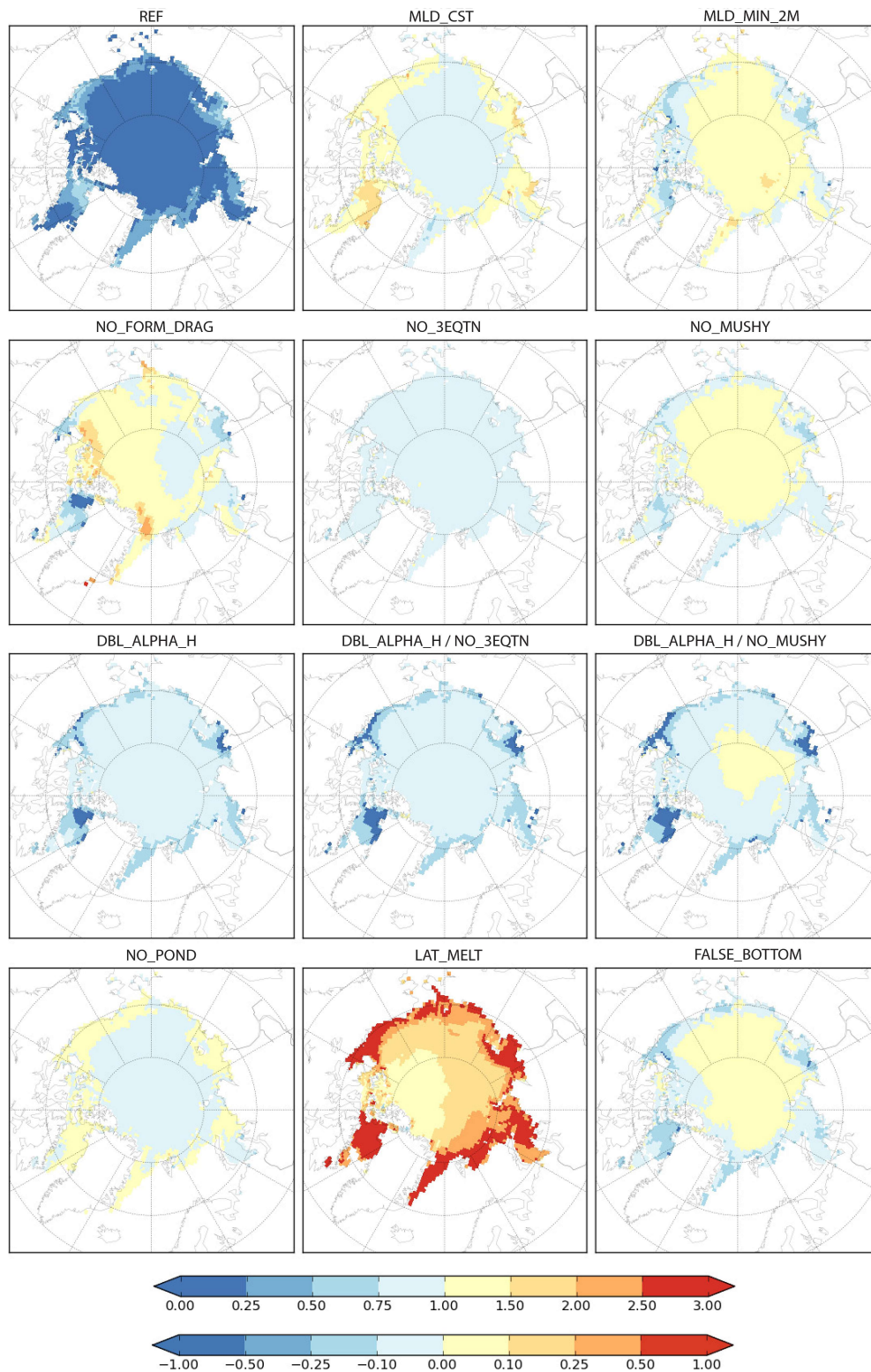


FIG. 7. Maps of the climatology of the average July lateral melt over the period 1994 to 2013 for all sensitivity runs. Note that the map for the *REF* model run is given in absolute melt rate values (in cm/day, top color bar) while all other model runs are given as difference in melt rate with respect to *REF* (in cm/day, bottom color bar).

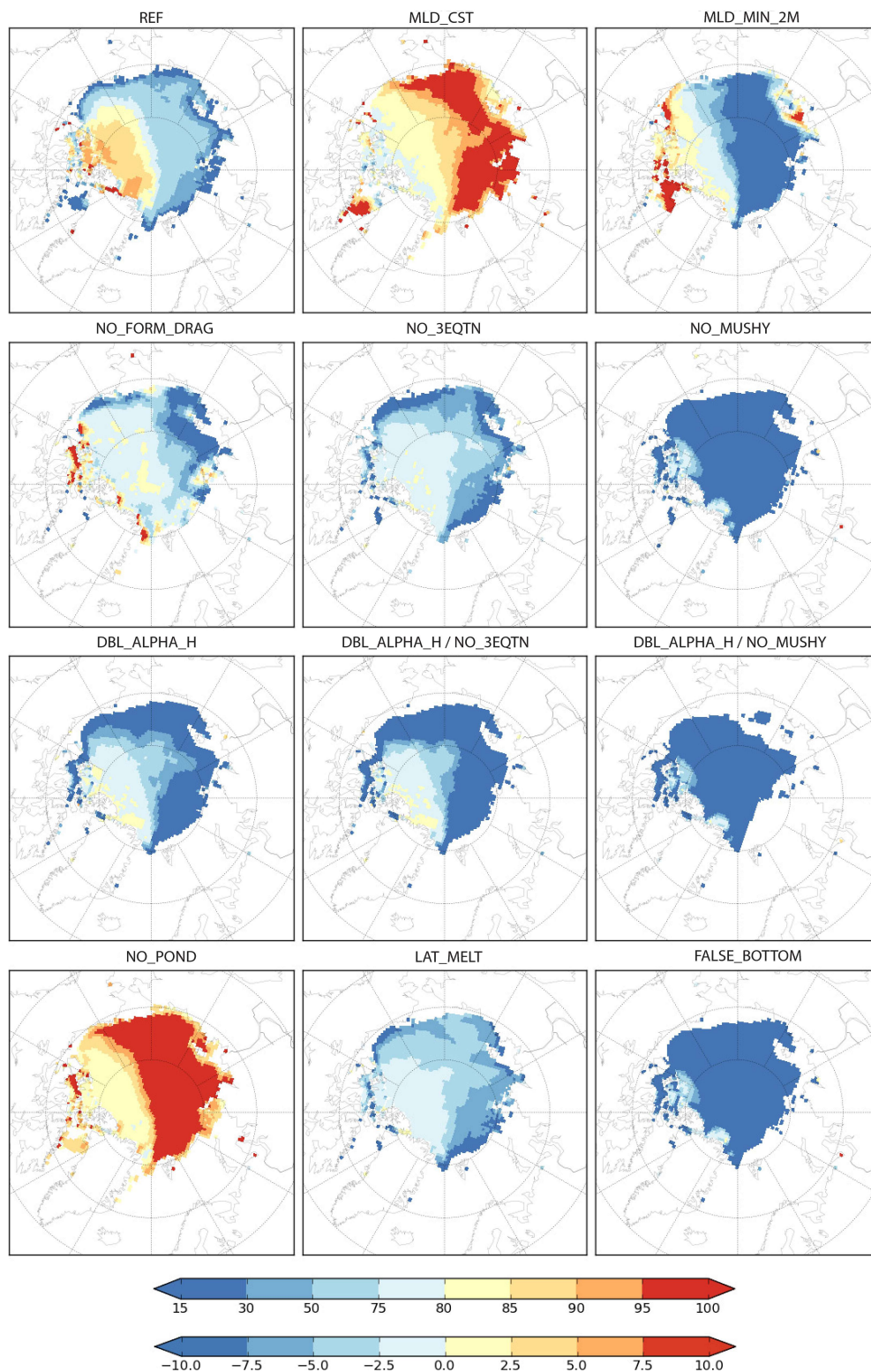


FIG. 8. August sea ice concentration climatology maps over the period 1994 to 2013 for all sensitivity runs. Note that the map for the *REF* model run is given in absolute concentration values (in %, top color bar) while all other model runs are given as difference in concentration with respect to *REF* (in %, bottom color bar).

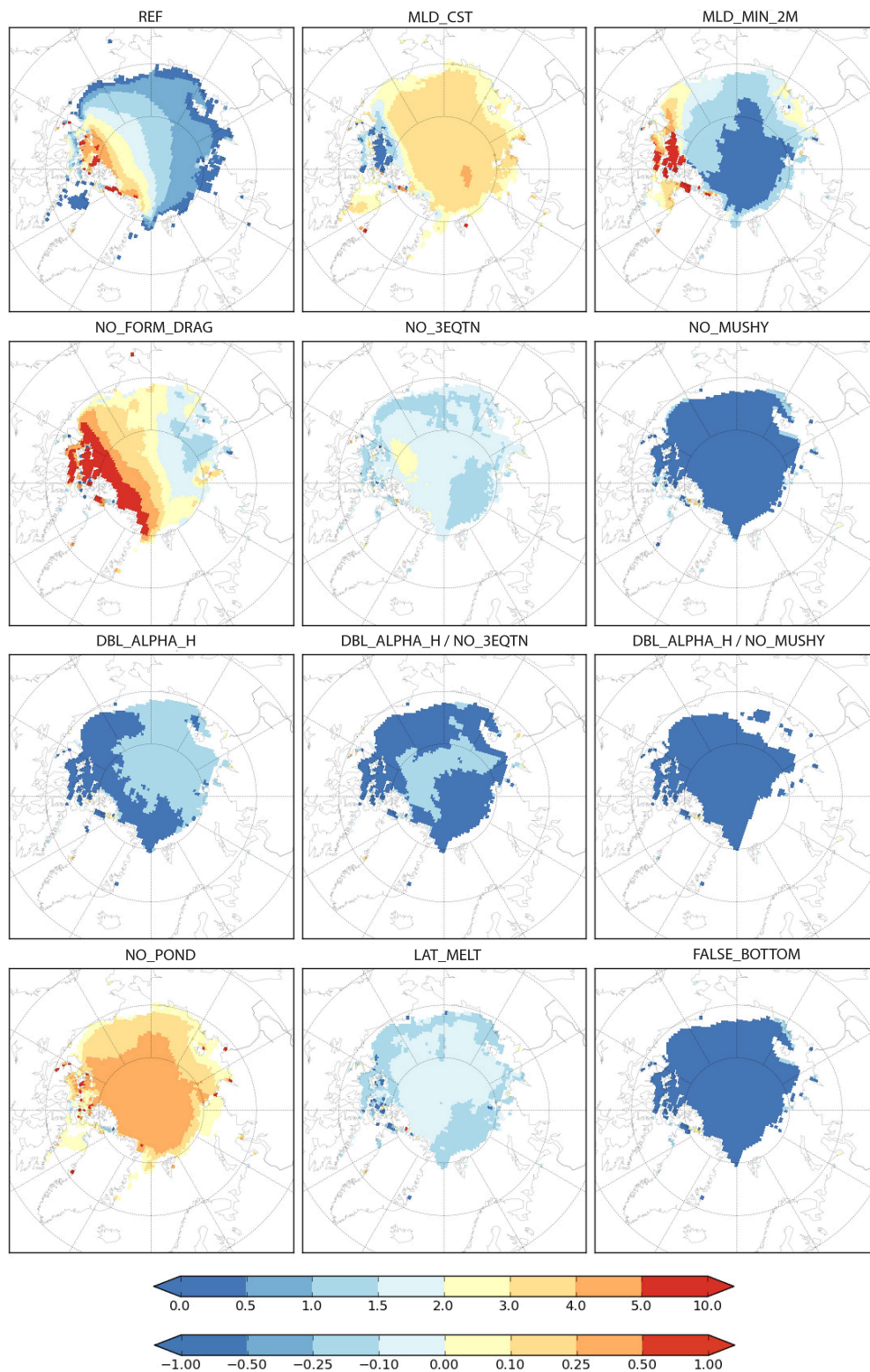


FIG. 9. August sea ice thickness climatology maps over the period 1994 to 2013 for all sensitivity runs. Note that the map for the *REF* model run is given in absolute thickness values (metres, in top color bar) while all other model runs are given as difference in thickness with respect to *REF* (metres, in bottom color bar).

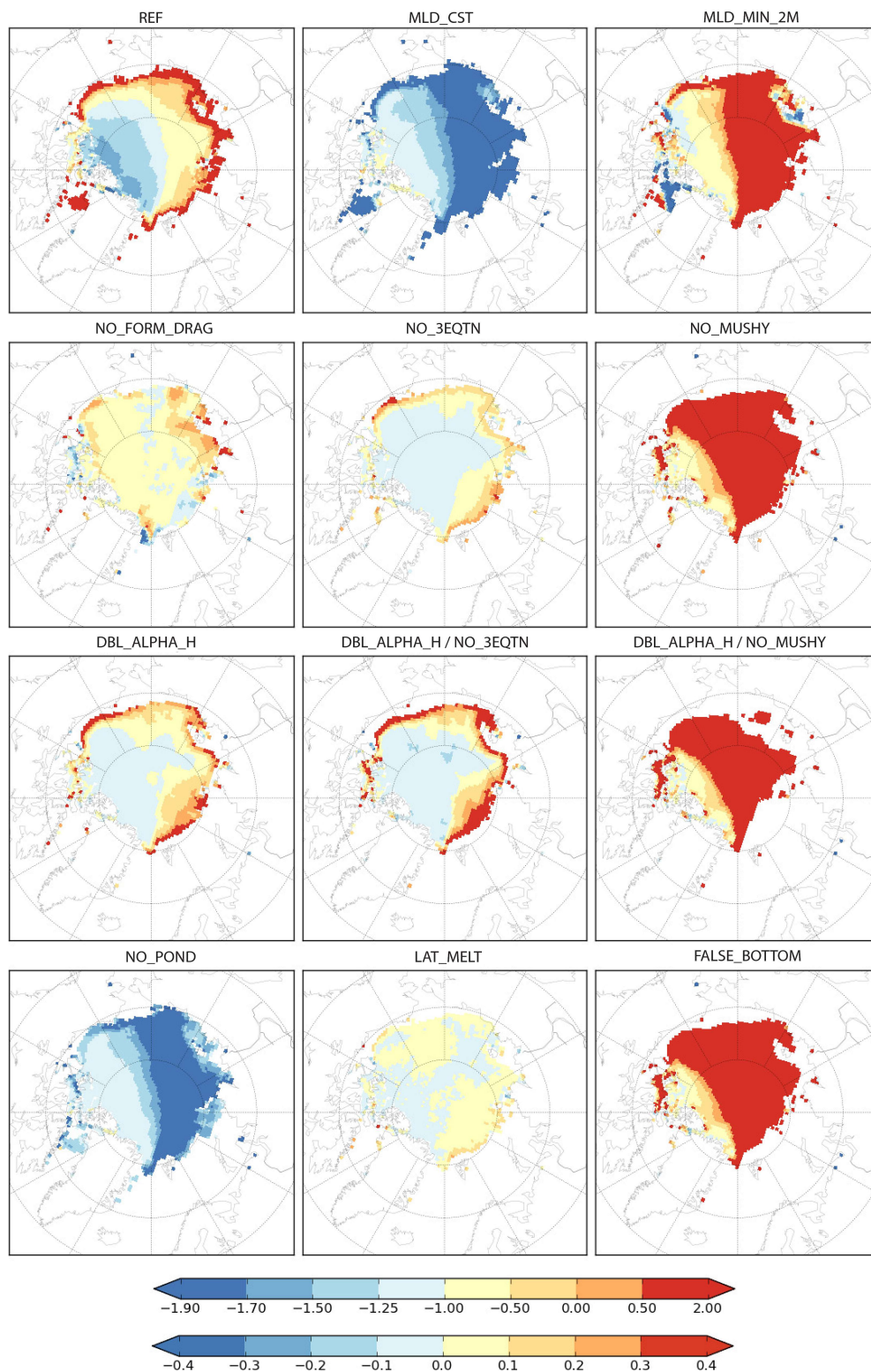


FIG. 10. August mixed layer temperature climatology maps over the period 1994 to 2013 for all sensitivity runs. Note that the map for the *REF* model run is given in absolute temperature values ($^{\circ}\text{C}$, in top color bar) while all other model runs are given in as difference in temperature with respect to *REF* ($^{\circ}\text{C}$, bottom color bar).

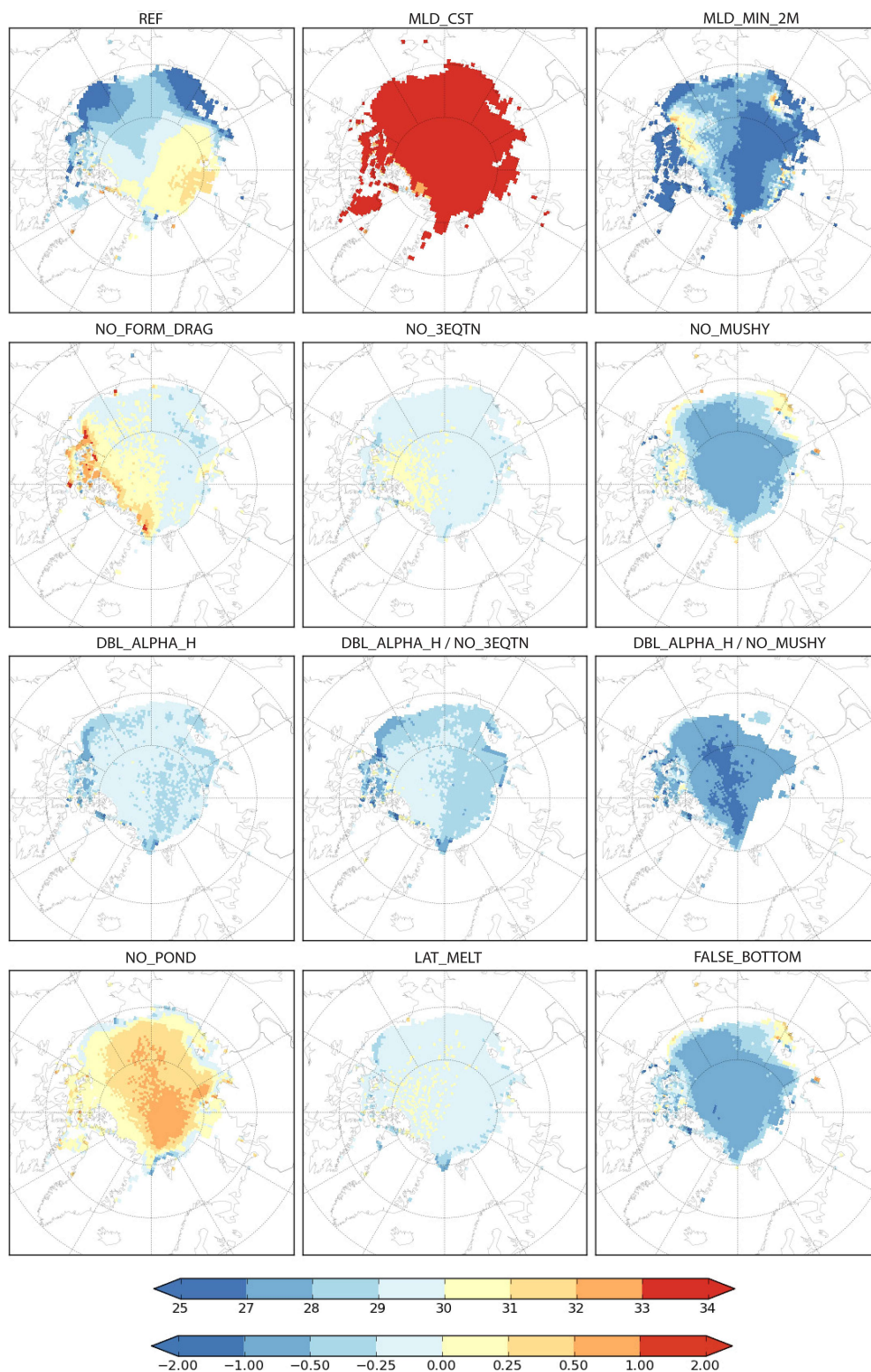


FIG. 11. August mixed layer salinity climatology maps over the period 1994 to 2013 for all sensitivity runs. Note that the map for the *REF* model run is given in absolute salinity values (PSU, top color bar) while all other model runs are given as difference in salinity with respect to *REF* (PSU, bottom color bar).

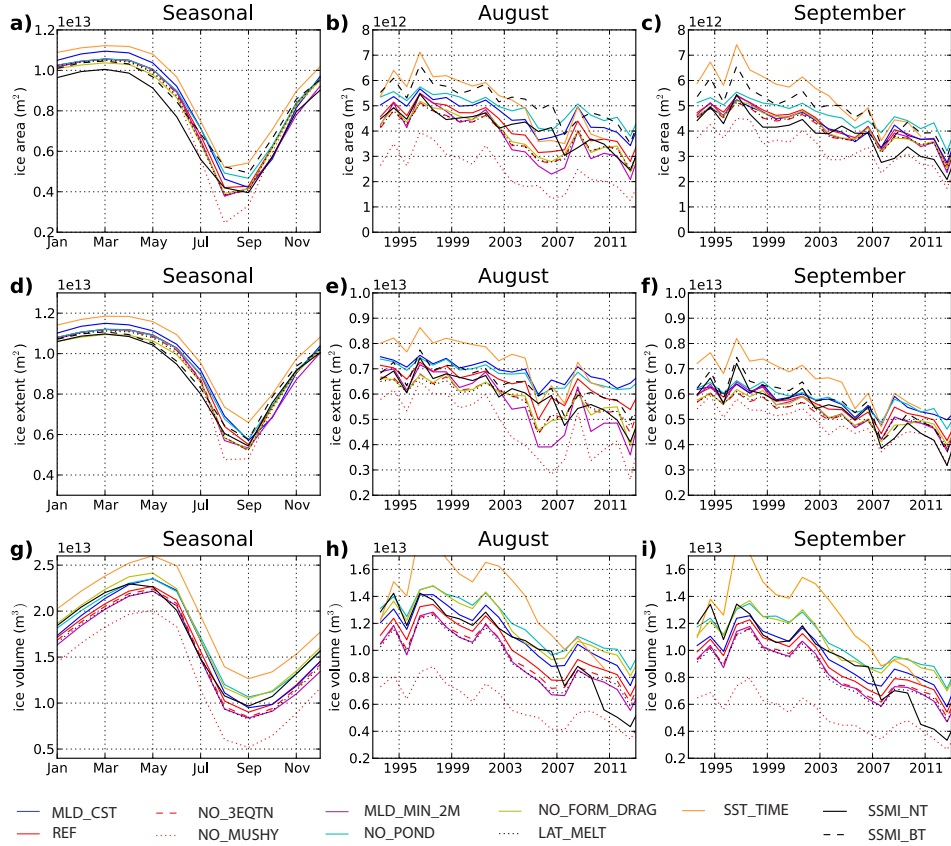


FIG. 12. Impact of the sensitivity model runs on the total area (a)-(c), total extent (d)-(f) and total volume (g)-(i) of sea ice. Figures on the first column show the seasonal climatology calculated over the period 1993 to 2012 while columns two and three show the time series for August and September. The colour code is as follows: *REF* in red, *MLD_CST* in blue, *SST_TIME* in green, *MLD_MIN_2M* in mauve, *SSMI_NT* and *PIOMAS* in solid black and *SSMI_BT* in dashed black.

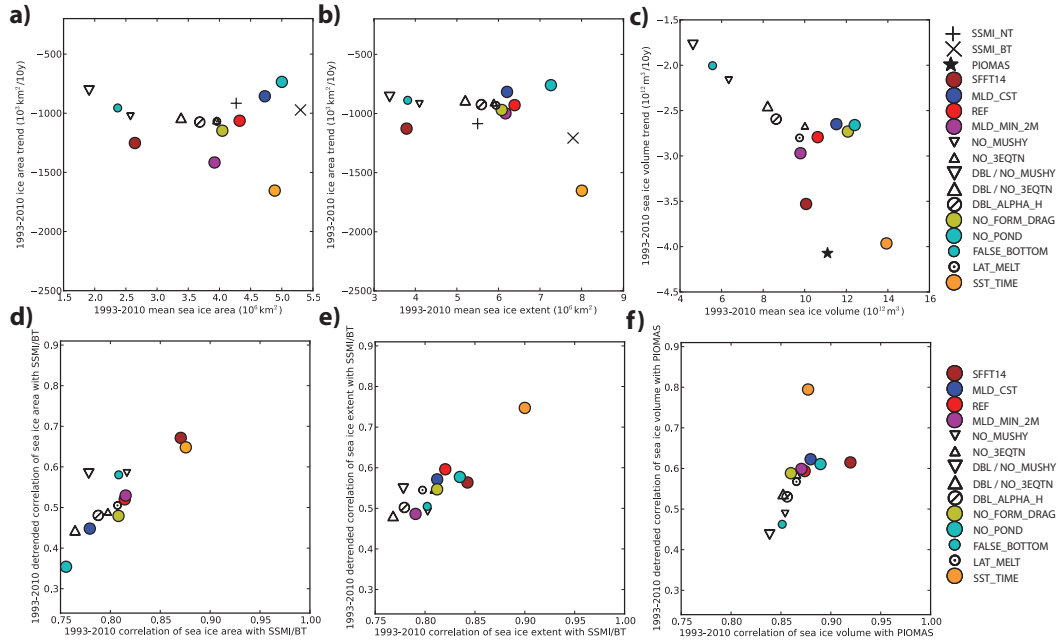


FIG. 13. Scatter plots of the trends vs averages over the period 1993 to 2010 of the August total sea ice area (a), sea ice extent (b) and sea ice volume (c). Scatter plots of the full and de-trended correlation coefficients between the model and observed time series of the total sea ice area (d), sea ice extent (d) and sea ice volume (f). Here we correlate model sea ice area and extent with the *SSMLBT* observation and model volume with *PIOMAS*. We show 13 model runs described in section 2. As a reference we also show values from the model run discussed in Schröder et al. (2014).

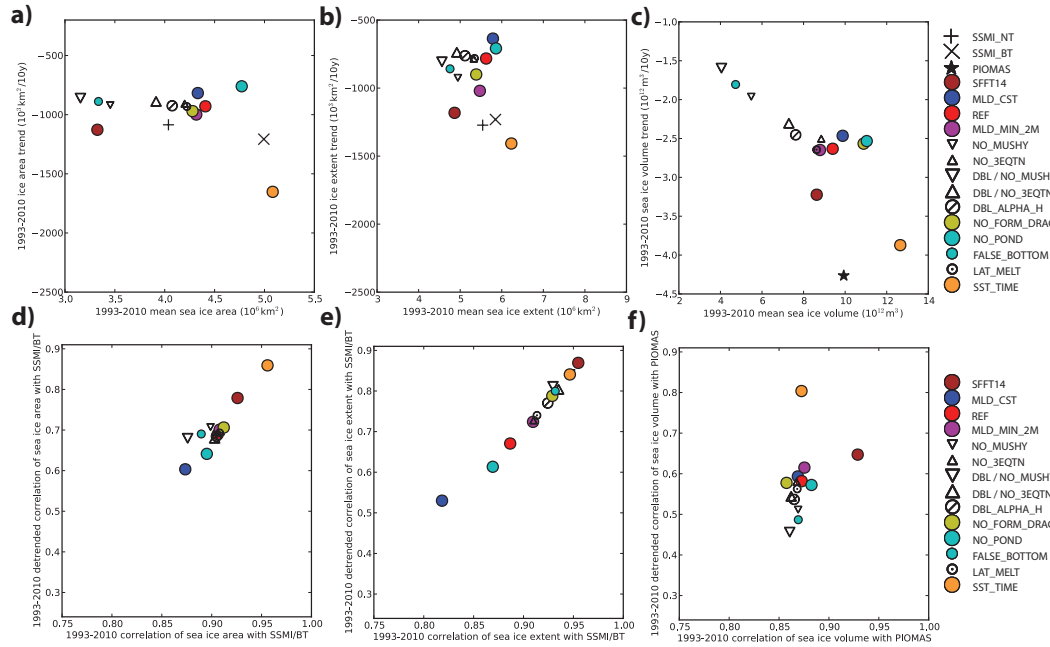


FIG. 14. Scatter plots of the trends vs averages over the period 1993 to 2010 of the September total sea ice area (a), sea ice extent (b) and sea ice volume (c). Scatter plots of the full and de-trended correlation coefficients between the model and observed time series of the total sea ice area (d), sea ice extent (e) and sea ice volume (f). Here we correlate model sea ice area and extent with the *SSMIBT* observation and model volume with *PIOMAS*. We show 13 model runs described in section 2. As a reference we also show values from the model run discussed in Schröder et al. (2014).